ФИЗИКА ЭЛЕМЕНТАРНЫХ ЧАСТИЦ И АТОМНОГО ЯДРА
2013. Т. 44. ВЫП. 4

COHERENT INSTABILITIES IN THE BOOSTER AND COLLIDER OF THE HEAVY ION ACCELERATOR COMPLEX NICA

D. Dinev

Institute for Nuclear Research and Nuclear Energy, Sofia

ФИЗИКА ЭЛЕМЕНТАРНЫХ ЧАСТИЦ И АТОМНОГО ЯДРА
2013. Т. 44. ВЫП. 4

COHERENT INSTABILITIES IN THE BOOSTER AND COLLIDER OF THE HEAVY ION ACCELERATOR COMPLEX NICA

D. Dinev

Institute for Nuclear Research and Nuclear Energy, Sofia

In the first part, some knowledge about the coherent instabilities in cyclic accelerators and storage rings necessary for the analysis of the collective effects in the heavy ion collider NICA is given. In the second part, the possibilities for arising of the coherent instabilities in the booster and in the collider of the NICA complex are discussed. Both coupling impedances and instability thresholds and growth rates have been estimated for single and coupled bunches. Parameters of the beam feedback system for damping the instabilities have been analyzed.

В первой части даются сведения о когерентных неустойчивостях в циклических ускорителях и в накопительных кольцах, необходимые для анализа коллективных эффектов в ускорительно-накопительном комплексе NICA. Во второй части обсуждаются возможности возникновения когерентных неустойчивостей в циклическом инжекторе-бустере и в коллайдере комплекса NICA. Приводятся оценки импедансов связи, порогов и скоростей развития неустойчивостей движения как одиночных сгустков, так и цепочек связанных сгустков. Анализируются параметры системы для подавления неустойчивостей с обратной связью по пучку.

PACS: 29.20.-c; 29.20.dk; 29.20.db

INTRODUCTION

For investigation of the nuclear matter at extreme conditions of very high temperatures and densities and search for the so-called mixed phase of the strongly interacting matter, the Nuclotron-based Ion Collider fAcility (NICA) will be built at the Joint Institute for Nuclear Research in Dubna. The accelerator complex NICA will include: new 6.2 MeV/u linac, a superconducting booster with maximum magnetic rigidity of 25 $\mathrm{T}\cdot\mathrm{m}$ and electron cooling, the upgraded superconducting synchrotron Nuclotron and two superconducting colliding rings with maximum magnetic rigidity of 45 $\mathrm{T}\cdot\mathrm{m}$ and systems for electron and stochastic cooling. The main goal of the NICA complex will be the generating of intense $(1.7\cdot 10^{10})$ ${}_{197}\mathrm{Au}^{79+}$ ion beams with energies between 1.0 and 4.5 GeV/u. There will be two interacting points. The luminosity is expected to be $1.0\cdot 10^{27}\ \mathrm{cm}^{-2}\cdot\mathrm{s}^{-1}$.

The paper is devoted to the problems of the coherent instabilities in the booster and in the collider of the NICA complex.

Coherent instabilities are one of the main phenomena limiting the performance of an accelerator. Hence, realistic estimation of all the factors that cause instability and of the instability threshold and growth rate is of big practical importance.

Sections 1–6 represent a short review of coherent instabilities in cyclic accelerators and storage rings. They give the reader all the necessary knowledge for understanding the next chapters, especially dedicated to the coherent instabilities in NICA.

Section 7 analyzes coherent instabilities in the cyclic injector-booster of the NICA accelerator complex. In Sec. 8, coherent instabilities in the collider rings are studied. Some recommendations for overcoming instabilities are given in Sec. 9. Parameters of the transverse and longitudinal feedback systems for damping of the injection errors and of the coupled bunch instabilities have been estimated, too.

1. WAKE FIELDS AND IMPEDANCES

Charged particles moving in a circular accelerator or a storage ring are themselves a source of EM fields. These EM fields add to the external EM fields which impose the designed particle trajectories. These self-fields are a superposition of EM fields generated by the beam in the free space and the EM fields produced by the image currents, induced by the beam on the walls of surrounding vacuum chamber or other devices such as: expansion bellows, connection flanges, pumping ports, RF cavities, beam position monitors, ferrite kickers, collimators, septum magnets, etc.

The EM fields produced by the beam and modified by the beam surroundings cause a force that acts back on the particles. For a beam with high intensity the self-EM-fields are strong enough to produce adverse effects like beam heating (increase of energy spread and bunch length) or even to give rise to an instability of the particle motion.

Following the principle of superposition in calculating the self-EM-fields, we can start with the simplest case of a point charge «e» moving with a constant velocity $v = \beta c$ in the machine vacuum chamber. If the material of the vacuum vessel is perfectly conducting the image, charge, induced on the inner surface of the chamber walls, will travel in pace with the source charge. In the realistic case of nonzero resistance of the walls or in the presence of wall discontinuities, the image current will lag behind the source charge. An EM field will be left behind the source particle. This field is called *wake field.* The wake field influences the motion of the trailing particles leading to energy loss, beam instabilities, or other undesirable effects.

In impulse approximation, when we are interested in the kicks experienced by the test particle, the wake field could be described by the so-called *wake function*. The concept of wake fields and impedances has been introduced by V. C. Vacaro

and A. M. Sessler in an effort to generalize all the cases of vacuum chamber wall geometry [1–3, 17–27]. To introduce the notion of wake function let us look at the following simplified model: a point source charge e and a test point charge q at a distance z behind ($z < 0$), both moving with constant velocity v along the chamber axis. The longitudinal wake function is defined as the potential seen by the test particle over a distance L, which is occupied by a RF cavity, expansion bellows or other kind of wall discontinuity, and produced by unit source charge:

$$w_{\parallel}(z) = -\frac{1}{e}\int_0^L E_s\left(s,\, t = \frac{s-z}{v}\right) ds. \tag{1}$$

The minus sign in (1) means that when we have deceleration of the test particle, the wake function is positive. For $z > 0$ and ultrarelativistic beams, $w_{\parallel}(z) = 0$ in accordance with the causality, i.e., the wake fields can affect only the trailing particles.

In transverse direction, the wake function is defined through the equation

$$\int_0^L F_{\perp}\left(s,\, t = \frac{s-z}{v}\right) ds = -q(ea)\, w_{\perp}(z), \tag{2}$$

where a is the transverse displacement of the source charge, so $D = ea$ is the dipole moment. The transverse kick that the test particle receives over the distance L is

$$\Delta\theta = \frac{v\,\Delta p_{\perp}}{E\,\beta^2} = \frac{\int_0^L F_{\perp}\, ds}{E\,\beta^2}. \tag{3}$$

Another approach to the collective effects is through the *coupling impedance.* The coupling impedance gathers in one quantity all the details of the electromagnetic interaction of the beam and its environment.

The longitudinal impedance is defined by the voltage $V(s,t)$ over a distance L seen by the particles:

$$V(s,t) = -I(s,t)\, Z_{\parallel}(\omega). \tag{4}$$

In (4) I is the beam current. By historical reasons the transverse coupling impedance is defined as

$$\int_0^L |\mathbf{E} + \mathbf{v}\times\mathbf{B}|_{\perp}(s,t)\, ds = -i\beta \int_{-\infty}^{\infty} Z_{\perp}(\omega)\, D(\omega, s)\, \mathrm{e}^{i\omega t}\, d\omega. \tag{5}$$

It could be proved that the coupling impedance is a Fourier transform of the wake function [24]

$$Z_{\parallel}(\omega) = \frac{1}{v}\int\limits_{-\infty}^{\infty} dz\, w_{\parallel}(z)\, \exp\left(-i\frac{\omega z}{v}\right), \tag{6}$$

$$Z_{\perp}(\omega) = \frac{i}{\beta v}\int\limits_{-\infty}^{\infty} dz\, w_{\perp}(z)\, \exp\left(-i\frac{\omega z}{v}\right). \tag{7}$$

2. SHORT-RANGE WAKE FIELDS

The short-range wake fields act over the bunch length (Fig. 1).

The effect of the short-range wake fields is in the potential-well distortion and in the increase of the longitudinal emittance.

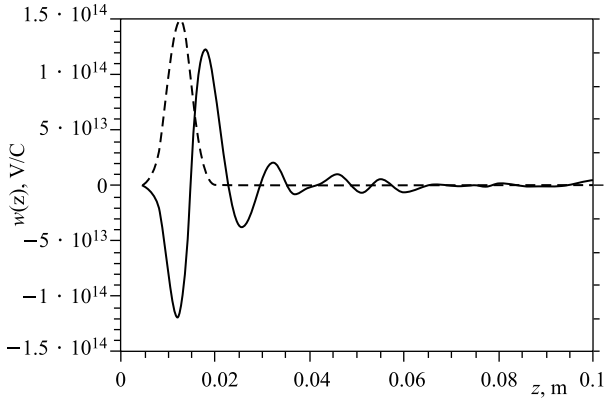

Fig. 1. Wake field of a 2.5 mm Gaussian bunch in DAFNE [69]

Wake fields with wavelengths short compared to the bunch length may induce microwave instabilities (MWI) in a single bunch. For specified beam intensity, the MWI limits the longitudinal impedances.

2.1. Wake Fields and Impedances of a Vacuum Chamber with Perfectly Conducting Walls with Uniform Cross Section (Case of Space Charge Dominated Beams). In the case of vacuum chamber with perfectly conducting walls of uniform cross section, the EM field generated by the source particle with charge e is the same as in the free space [24]:

$$4\pi\varepsilon_0\mathbf{E} = \frac{e\mathbf{r}}{\gamma^2 r^3}\,\frac{1}{(1-\beta^2\,\sin^2\,\theta)^{3/2}}, \quad \mathbf{H} = \frac{1}{Z_0}\,(\mathbf{v}\times\mathbf{E}), \tag{8}$$

where

$$Z_0 = 376.73\ \Omega \tag{9}$$

is the free-space impedance; $\mathbf{r}$ is the radius-vector from the source charge to the test point, and θ is the angle between the radius-vector and the velocity.

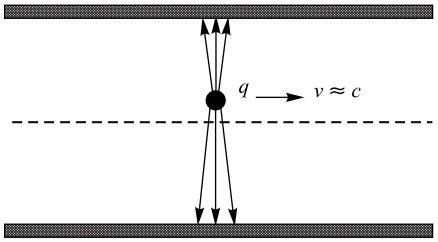

Fig. 2. EM field of ultrarelativistic charge moving in a perfectly conducting pipe

In the ultrarelativistic case ($v \to c$), the field is pancake-like (Fig. 2), i.e., it is nonzero in the interval of angles $\Delta\theta \sim 1/\gamma$ around the perpendicular to the particle velocity. There are no forces acting on the test particle and the wake function vanishes as $1/\gamma^2$.

a) *In Longitudinal Direction.* The longitudinal wake function is [26]

$$w_{\parallel}^{\mathrm{sc}}(z) = \frac{1}{\omega_0}\frac{Z_0}{4\gamma^2\beta}\, g\delta'\left(\frac{z}{v}\right). \tag{10}$$

The longitudinal space-charge impedance is [17–33]

$$Z_{\parallel}^{\mathrm{sc}}(\omega) = -\frac{iZ_0 g}{2\beta\gamma^2}\frac{\omega}{\omega_0}, \tag{11}$$

$$g = 1 + 2\,\ln\left(\frac{b}{a}\right), \tag{12}$$

where a is the beam radius; b is the vacuum chamber radius; ω_0 is the synchronous angular revolution frequency.

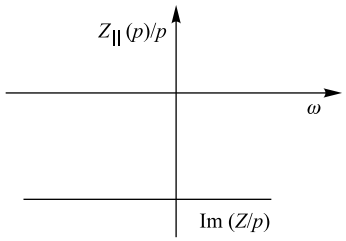

Fig. 3. Longitudinal space-charge impedance $Z_{\parallel}(p)/p$, $p = \omega/\omega_0$

The space-charge impedance is purely reactive (negative inductance) (Fig. 3), i.e., there is no energy loss during the particle motion.

Let us remember that the derivative of the impulse δ-function has the property

$$\int_a^b \varphi(x)\,\delta'(u-x)\,dx = -\int_a^b \varphi(x)\,\delta'(x-u)\,dx = \varphi'(u). \tag{13}$$

For elliptical vacuum pipe and ultrarelativistic particles, an equivalent pipe radius $b_{\rm eq}$ is introduced [24]. This equivalent radius is function of the elliptical parameter

$$\bar{q} = \frac{h-b}{h+b}, \tag{14}$$

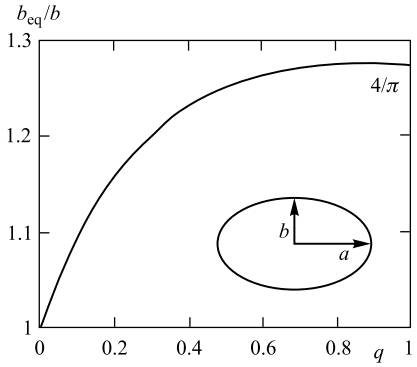

Fig. 4. Normalized equivalent radius for an elliptical vacuum pipe

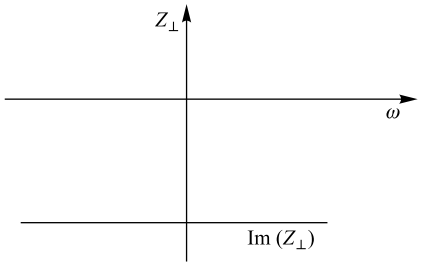

Fig. 5. Transverse space-charge impedance $Z_\perp$

where h and b are the pipe half-width and half-height (Fig. 4).

For a rectangular beam pipe with a full height h and full width w [53]:

$$\frac{Z_\parallel(\omega)}{n} = -j\frac{Z_0}{2\beta\gamma^2}\times$$
$$\times\left[1+2\ln\left(\frac{2h}{\pi a}\tanh\left(\frac{\pi\omega}{2h}\right)\right)\right]. \tag{15}$$

b) *In Transverse Direction.* The transverse wake function is [26]

$$w_\perp(z) = \frac{Z_0 cL}{2\pi\gamma^2}\left(\frac{1}{a^2}-\frac{1}{b^2}\right)\delta(z). \tag{16}$$

The transverse space-charge impedance is [17–33]

$$Z_\perp^{\rm sc}(\omega) = -\frac{i\,R\,Z_0}{\beta_0^2\gamma_0^2}\left(\frac{1}{a^2}-\frac{1}{b^2}\right), \tag{17}$$

R being the machine mean radius (Fig. 5).

For a rectangular beam pipe [53],

$$Z_\perp^{\rm sc}(\omega) = -j\frac{RZ_0}{\beta^2\gamma^2}\left[\frac{1}{a^2}-\frac{8}{h^2}(\xi_1-\varepsilon_1)\right], \tag{18}$$

where ξ_1 and ε_1 are the coefficients that are found by conformal mapping technique. For the ratio $w/h = 2.5$, we have $\xi_1^H - \varepsilon_1^H = 0.208$ and $\xi_1^V - \varepsilon_1^V = 0.411$.

The lower the particle energy the higher the space-charge impedance. The space-charge impedance could be very large for low velocities (low β). Thus, for 50 MeV protons $\beta = 0.3$ and $Z_\parallel^{\rm sc}/n$ could reach 1.5 kΩ.

In AGS booster, the space-charge contribution is $Z_\parallel/n = j\,27.5\ \Omega$ for the longitudinal direction and $Z_\perp = j\,9.2$ MΩ/m for protons in transverse direction and $Z_\perp = j\,2018$ MΩ/m for Au ions in transverse direction [15].

In SIS-10, the space-charge impedance is expected to be [58]: $Z_\parallel/n = j\,180\ \Omega$ and $Z_\perp = j\,80$ MΩ/m.

2.2. Broad-Band Impedance. Changes of vacuum chamber aperture such as bellows, flanges, beam position monitors, kickers, gate valves, vacuum ports, beam collimators, etc., can trap some magnetic field (Fig. 6).

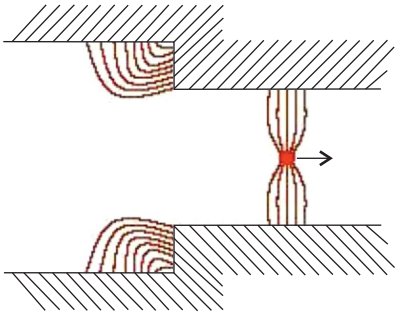

Fig. 6. Discontinuity of the vacuum chamber

The measurements on many existing machines show that such structures are well approximated by a Broad-Band (BB) resonator with a quality factor $Q \sim 1$ and a resonant frequency ω_r around the vacuum chamber pipe cut-off frequency (~ 1 GHz) [17–33, 62, 63, 66, 69]. This is illustrated by Fig. 7.

At low frequencies

$$\frac{Z_{\parallel\,\mathrm{BB}}(\omega)}{n} = j\,R_{\mathrm{sh}}\frac{\omega_0}{\omega_r}, \qquad (19)$$

where the resonance frequency ω_r is taken to be equal to the pipe cut-off frequency

$$\omega_r \approx \omega_{\text{cut-off}} = \frac{c}{b}. \qquad (20)$$

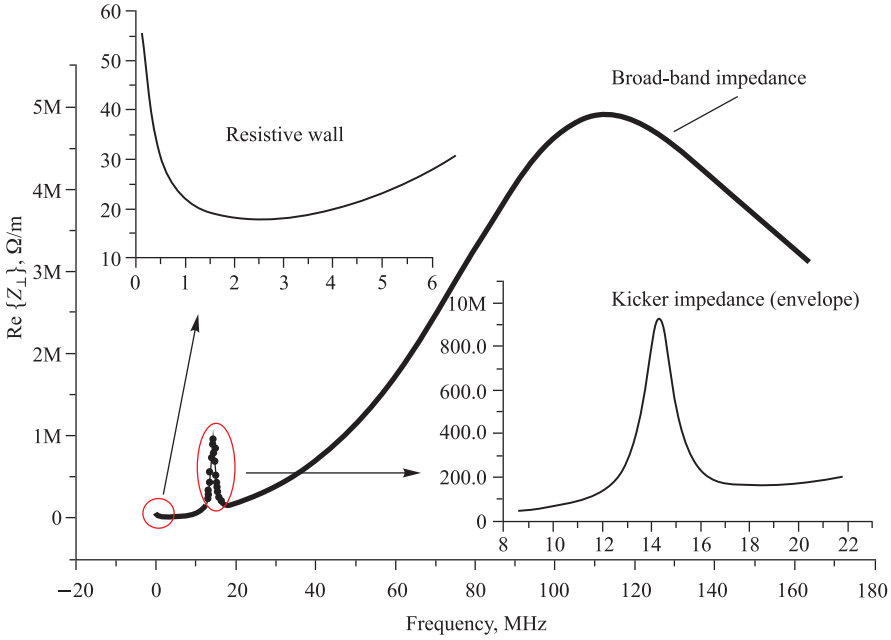

Fig. 7. Real part of the transverse broad-band impedance in SIS-18 at injection energy of 11.4 MeV/u. The resistive wall and kicker impedances are most important at low frequencies. The broad-band impedance is dominant for higher frequencies [42]

The quality factor Q is taken to be equal to unity and the shunt impedance $R_{\rm sh}$ is usually taken to be 60 Ω:

$$Z_{\parallel\,\mathrm{BB}}(\omega) = \frac{60\ \Omega}{1 + i\left(\dfrac{c}{b\omega} - \dfrac{b\omega}{c}\right)}. \tag{21}$$

At low frequencies, the broad-band impedance is

$$\frac{Z_{\parallel\,\mathrm{BB}}(\omega)}{n} = j\,\frac{376.73 b\beta}{C}\,\Omega, \tag{22}$$

where C is the accelerator circumference.

The BB impedance is inductive impedance, approximately constant for low frequencies end. The BB resonator has an impedance curve with large bandwidth ($1/\delta f \ll T_0/M$), M — number of bunches, and therefore the wake field decays rapidly. This element represents local interactions which can couple only close particles.

For a well-designed machine,

$$\frac{Z_{\parallel\,\mathrm{BB}}\,(\omega)}{n} \leqslant 1\ \Omega. \tag{23}$$

The number of generic broad-band resonators at unit accelerator length for a sufficiently smooth vacuum chamber is given by

$$\frac{n_{\mathrm{BB\,cavities}}}{C} \leqslant \frac{1}{376.73\, b}. \tag{24}$$

This gives a crude estimate of the required smoothness of the accelerator vacuum chamber.

In Fig. 8, the total broadband impedance $|Z_\parallel/n|$ up to 3 GHz in RHIC is shown.

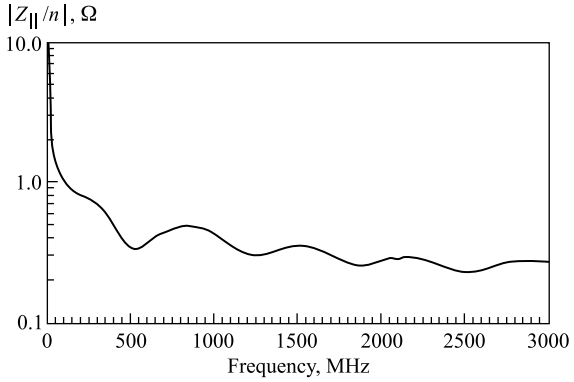

Fig. 8. Total broad-band impedance in RHIC [49]

At very low frequencies, up to about 100 MHz, main contribution is from the beam chamber wall impedance and beam position monitors. At high frequencies, the impedance falls to $0.25\ \Omega$. At frequencies up to 1.5 GHz, the main contribution is from the kickers. Above 1.5 GHz, all the other devices make a contribution: aperture transitions, expansion bellows, BPMs, gate valves, vacuum ports, collimators, etc.

In transverse direction the broad-band impedance could be calculated through the longitudinal broad-band impedance [24]:

$$Z_{\perp\,\mathrm{BB}} = \frac{2R}{\beta_0 b^2}\,\frac{Z_{\parallel\,\mathrm{BB}}}{n} = \frac{2c}{b^2}\,\frac{Z_{\parallel\,\mathrm{BB}}}{n\omega_0}. \tag{25}$$

2.3. Aperture Transitions. For the case of aperture transition $r_1 \to r_2$ ($\Delta = r_2 - r_1$, half-angle $= \theta$) [49]:

$$\frac{Z_{\parallel\,\mathrm{ap,\,tr}}(\omega)}{n} = -Z_0\frac{3}{2C}\,\left(\frac{r_1\Delta^2}{r_2^2}\right)\left(\frac{2\theta}{\pi}\right)^{1/2}. \tag{26}$$

Two cases could be distinguished: a particle exiting into a pipe of a bigger radius, which is called step-out case, and a particle entering a narrow pipe, which is called step-in case. Theoretical analysis shows that the longitudinal coupling impedance is mostly resistive in the step-out case with a big contribution at high frequencies above cut off. In the step-in case the longitudinal coupling impedance is low and vanishes at high frequencies (Fig. 9).

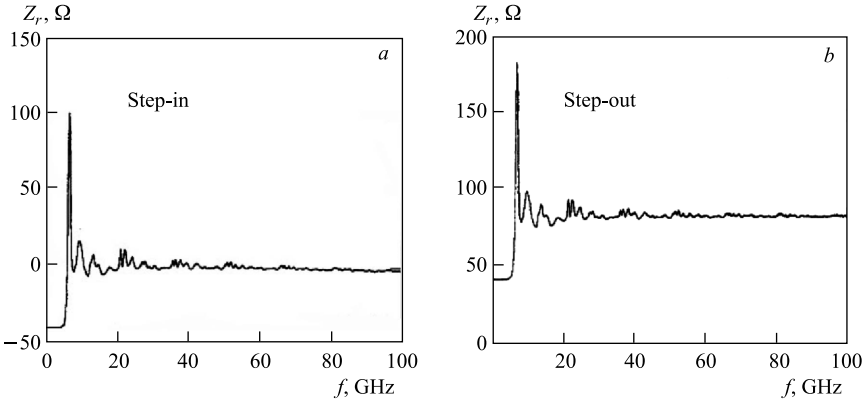

Fig. 9. Longitudinal coupling impedance of vacuum pipe discontinuity [18]

Instead of making an abrupt step between two beam pipes of different radii, it is desirable to make the aperture transition more gradual using a conical section of the beam pipe. In this case, the following rule of thumbs is applied — the taper length must be five times longer than the difference in the pipe radii («five-to-one rule»).

In RHIC, all the vacuum pipe transitions are tapered with a transition length at least five times as long as the change in pipe radius. The vacuum ports, gate valves and collimators are shielded.

2.4. Bellows. For a bellow with N rectangular corrugations of length g and depth Δ [49]:

$$\frac{Z_{\parallel\,\mathrm{bel}}}{n} = -jZ_0\frac{N}{C}\left(\frac{g\Delta}{b}\right). \tag{27}$$

The estimate (12) has 20% accuracy. If the bellows are left unshielded, they will dominate the BB impedance. In RHIC, the bellows contribute $Z_\parallel(\omega)/n = -1.01j,\,\Omega$ if they are left unshielded and $Z_\parallel(\omega)/n = -0.02j,\Omega$ when all the bellows are carefully shielded.

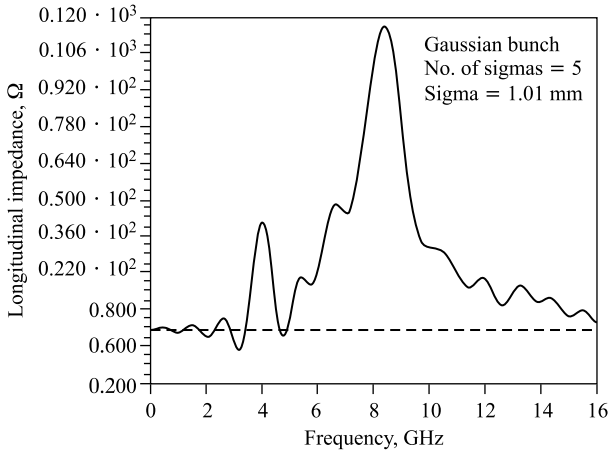

Fig. 10. Real part of the longitudinal impedance of a circular bellow with 10 convolutions [53]

Figure 10 shows example of longitudinal coupling impedance of bellows in Fermilab Main Injector. For a single bellow it could be characterized approximately as the impedance of two resonators with low quality factors and resonant frequencies in the GHz region.

2.5. Kickers. The kickers have large contribution to the longitudinal impedance for frequencies up to 750 MHz (Fig. 11). The kicker represents a transmission line with ferrite filling [67]. For low frequencies (up to 50 MHz) the coupling impedance is given by [49]

$$\frac{Z_{\parallel\,\mathrm{kick}}(\omega)}{n} = \frac{Z_0}{4n}\left\{\left[1-\cos\left(2\pi\frac{f}{f_0}\right)\right] - j\left[2\pi\frac{f}{f_0} - \sin\left(2\pi\frac{f}{f_0}\right)\right]\right\}, \tag{28}$$

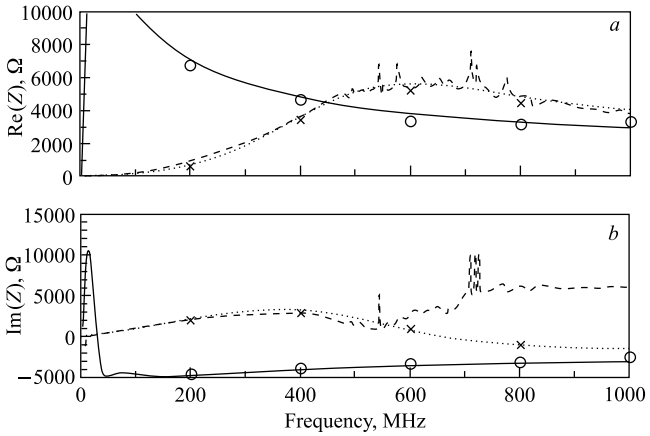

Fig. 11. Longitudinal coupling impedance of the SPS MKE kicker; dashed lines — analytical results, dotted lines — measurement by the wire method [67]

Z_0 is the characteristic impedance of the line, and f_0 is the resonance frequency:

$$f_0 = \frac{Z_0 w}{\mu_0 h l}, \tag{29}$$

h is the kicker half-height; w is kicker half-width.

In AGS booster, the contribution of the injection, extraction and abort kickers is small: $Z_\parallel/n = 0.16\ \Omega$ and $Z_\perp = 0.002\ \mathrm{M\Omega/m}$ [15].

In SIS-100, the contribution of the ferrite loaded extraction kickers will be [58] $Z_\perp = 0.5\ \mathrm{M\Omega/m}$.

2.6. C-Type Kickers.

$$Z_{\parallel\,\mathrm{kick}} = \frac{\omega^2 \mu_0^2 l^2 h^2}{4b^2(j\omega L + Z_{\mathrm{cable}})}, \tag{30}$$

$$Z_{\perp\,\mathrm{kick}} = \frac{c\omega \mu_0^2 l^2}{4b^2(j\omega L + Z_{\mathrm{cable}})}, \tag{31}$$

where h is the height; l — the length; Z_{cable} — the cable impedance, and L — the inductance.

In RHIC, the dominant contribution to broad-band impedance is expected to be from the injection kickers. There are four 1.1 m long C-shaped kickers, with no shielding $Z_\parallel/n \leqslant 0.25\ \Omega$.

3. LONG-RANGE WAKE FIELDS

The long-range wake fields act on many bunches or even on many turns. The most popular source of long-range wake fields is the high Q resonant structures:

the fundamental and the higher order modes in the RF cavities. They can produce Robinson and coupled bunch instabilities.

3.1. Resistive Walls. If the vacuum chamber is made of a material with finite conductivity, the charged particle will lag an EM wake field behind it. Close to the particle, this wake field must be decelerating as the source particle dissipates some of its kinetic energy exciting currents in the vacuum chamber walls. The longitudinal wake field is shown in Fig. 12.

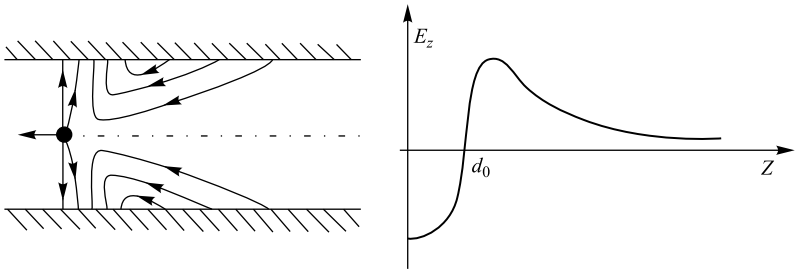

Fig. 12. EM wake field in vacuum pipe with finite conductivity

The characteristic distance is [24]

$$d_0 = \sqrt[3]{\frac{b^2}{Z_0\sigma}}, \tag{32}$$

where b is the pipe radius; σ is the conductivity.

At distances bigger than d_0 behind the source particle, the EM field is accelerating for the trailing particles of the same charge sign, while at distances less than d_0 it is decelerating in agreement with the energy balance condition.

Immediately behind the source particle in ultrarelativistic case,

$$E_z = -\frac{q}{\pi\varepsilon_0 b^2}. \tag{33}$$

At long distances,

$$E_z = \frac{q}{4\pi\varepsilon_0 b}\sqrt{\frac{1}{\pi Z_0\sigma}}\,\frac{1}{|z|^{3/2}}. \tag{34}$$

The tail of the wake field extends to $d_0 + \sigma Z_0 b^2$.

a) *In Longitudinal Direction.* At distances higher than d_0, the longitudinal wake function decays slowly. The long tail is described by the formula [24]:

$$w_\parallel(z) = -C\frac{c\beta^{3/2}}{4\pi b}\sqrt{\frac{Z_0}{\pi\sigma}}\,\frac{1}{|z|^{3/2}},\ [\Omega/\mathrm{s}], \tag{35}$$

where C — machine circumference; c — light speed, $\beta = v/c$.

The above expression fails for small distances. Just behind the source particle, the wake function changes the sign (Fig. 13).

For $|z| \ll d_0$, $w_\parallel(z) > 0$ which means deceleration of the trailing particles. This is in accordance with the energy saving law.

In longitudinal direction, the coupling impedance is [17–33]

$$Z_\parallel^{\mathrm{rw}}(\omega) = (1+i)\,\frac{Z_0\,\beta\,\delta}{2b}\,\frac{\omega}{\omega_0}, \quad (36)$$

where δ is the skin depth

$$\delta = \sqrt{\frac{2}{\mu\sigma\omega}}. \quad (37)$$

The resistive wall impedance is peaked at low frequencies (dominates up to 100 MHz). It is not a problem in the longitudinal direction, but it is in the transverse direction (Fig. 14).

b) *In Transverse Direction.* The transverse wake function for distances much longer than d_0 is [24]

$$w_\perp(z) = -C\frac{c\beta^{3/2}}{\pi b^3}\sqrt{\frac{Z_0}{\pi\sigma}}\frac{1}{|z|^{1/2}}. \quad (38)$$

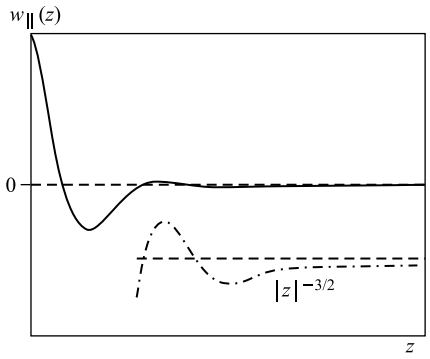

Fig. 13. Longitudinal wake function of a lossy vacuum pipe

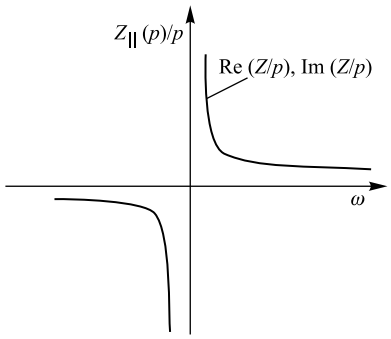

Fig. 14. Longitudinal resistive wall impedance

In transverse direction, the coupling impedance could be calculated applying the relation between the transverse and longitudinal impedances [17–33]:

$$Z_\perp = \frac{2c}{b^2}\,\frac{Z_\parallel}{\omega}, \quad (39)$$

$$Z_\perp^{\mathrm{rw}} = (1+i)\,\frac{R\,Z_0}{b^3}\,\delta. \quad (40)$$

The most important effect of the resistive walls is the transverse coupled bunch mode at low frequencies and low energies.

In AGS booster, the contribution of the resistive walls is $Z_\parallel/n = (1+j)\times(0.33/\sqrt{n})\ \Omega$ for the longitudinal direction and $Z_\perp = (1+j)(1.2/\sqrt{n})$ MΩ/m for the transverse direction [15]. These impedances are too small in the microwave region to drive a fast instability.

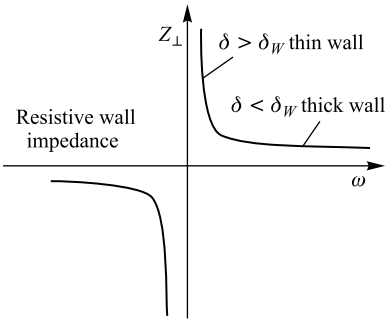

Fig. 15. Transverse resistive wall impedance

In RHIC, the contribution of the resistive walls is $Z_\parallel = (1+j)\sqrt{f}\,748\ \Omega$, where the frequency is in GHz.

In SIS-100, the resistive wall impedance will be [58]: $Z_\parallel/n = 7 - j\ \Omega$ and $Z_\perp = 0.4$ MΩ/m. It is expected to be the main source of transverse instability (Fig. 15).

3.2. Narrow-Band Resonant Element. The EM fields generated by the beam in the RF cavities are between the main sources of beam-environment interaction [17–33, 72–74, 82]. Instead of the fundamental mode at frequency $\omega_{\rm RF} = h\omega_0$, accelerating cavities have many other sharp resonances corresponding to all the resonant modes of the RF structure (higher-order modes, HOMs) (Fig. 16). When a bunch passes through the cavity it could excite these parasitic modes.

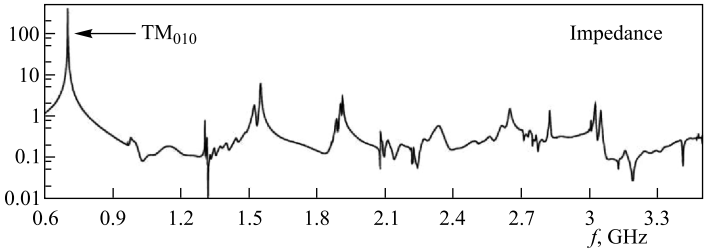

Fig. 16. Impedance spectrum of five-cell superconducting cavity for the electron cooling project at RHIC [72]

The longitudinal wake function of a RF cavity is [17–19]

$$w_\parallel(z) = \frac{\omega_r R_{\rm sh}}{Q}\,\exp\left(\frac{\alpha z}{v}\right)\left[\cos\left(\frac{\bar\omega z}{v}\right) + \frac{\alpha}{\omega}\,\sin\left(\frac{\bar\omega z}{v}\right)\right], \tag{41}$$

where ω_r is the resonant frequency; $R_{\rm sh}$ is the shunt impedance,

$$\alpha = \frac{\omega_r}{2Q}, \tag{42}$$

$$\bar\omega^2 = \omega_r^2 - \alpha^2. \tag{43}$$

This wake field oscillates in z with a wavelength equal to

$$\lambda_{\rm RF} = \frac{2\pi c}{\omega_r}. \tag{44}$$

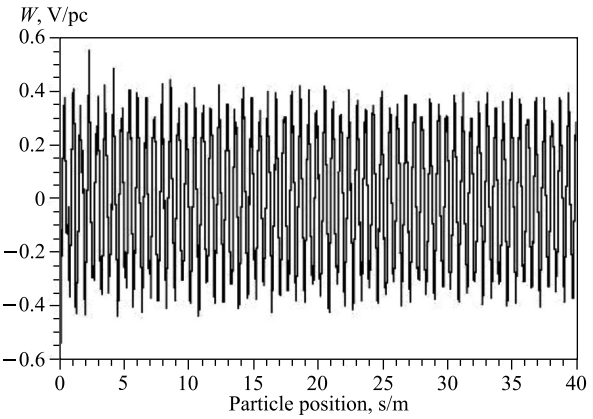

Fig. 17. Long-range wake fields in the PEP-II RF cavity [73]

It is damped to $1/e$ at a distance $(Q\pi)\lambda_{\mathrm{RF}}$. The RF cavity wake oscillates and damps very slowly with z (Fig. 17).

The field in the resonant element decays as $\exp\left(-\dfrac{\omega_r}{2Q}\,t\right)$, where ω_r is the resonance frequency and Q is the quality factor. A time $t = 2Q/\omega_r$ is needed for the excited field to reduce e times. As in the RF cavities, the quality factor Q is very high, 10^4 or higher, this field lasts long enough to couple the successive bunches circulating around the ring (Fig. 18).

The longitudinal coupling impedance of a resonator is [17–33]

$$Z_{\parallel} = \frac{R_{\mathrm{sh}}}{1 + iQ\left(\dfrac{\omega}{\omega_r} - \dfrac{\omega_r}{\omega}\right)}, \tag{45}$$

where R_{sh} is the shunt impedance of the resonator.

Below resonant frequency ($\omega \ll \omega_r$) the impedance is pure inductance; at resonance ($\omega = \omega_r$) — pure resistance, and above transition ($\omega \gg \omega_r$) — pure capacitance. The bandwidth (HWHM) is

$$\delta\,\omega = \frac{\omega_r}{2Q}. \tag{46}$$

If in the accelerator there are many bunches, the attenuation between two successive bunches is given by $\exp(-\alpha)$, where

$$\alpha = \pi\,\frac{f_r t_{\text{bunch-bunch}}}{Q}. \tag{47}$$

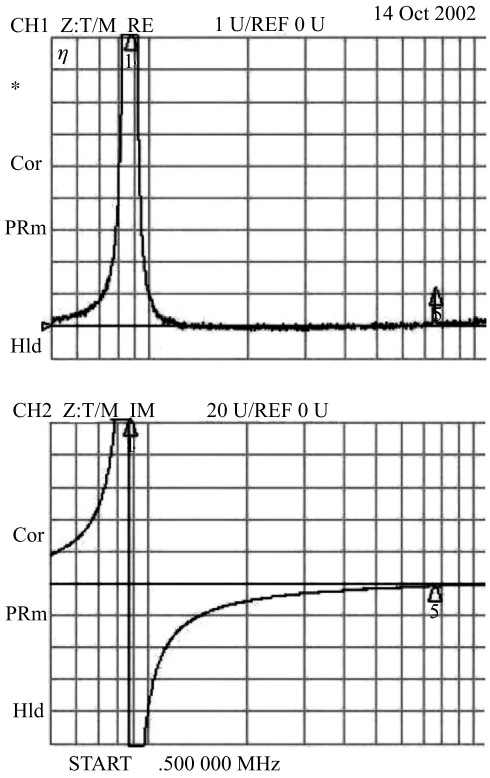

Fig. 18. Longitudinal impedance of SNS RF cavity [74]

In the case of high Q (narrow band) resonator, the decay of the wake field is slow ($\alpha \ll 1$). Such a long-range wake field is a source of bunch coupling. Wake field of a narrow-band resonator lasts long time and successive bunches will be coupled by such a resonator.

4. SINGLE-BUNCH INSTABILITIES

4.1. Microwave Instability. This is an instability of individual bunches at very high frequencies, in the GHz region [4–6, 9, 15, 81]. This is a fast instability, i.e., the growth rate is much larger than the synchrotron frequency.

In longitudinal direction, the stability criterion is [49]

$$\left|\frac{Z_{\parallel}(\omega)}{n}\right| \leqslant \frac{2\pi\beta^2\gamma E_0\, A\,|\eta|\,(\Delta p/p)^2}{eZI_{\mathrm{peak}}}, \tag{48}$$

or

$$\left|\frac{Z_{\parallel}(\omega)}{n}\right| \leqslant \frac{\sqrt{2\pi}V_{\mathrm{RF}}\left|\cos\left(\phi_S\right)\right|\sigma_\phi^3}{h^2 N_b e Z \omega_0}, \tag{49}$$

or [53]

$$\left|\frac{Z_{\parallel}\left(\omega\right)}{n}\right| \leqslant \frac{2\pi}{\beta^5 e Z I_b}\left(\frac{\omega_0 S}{6\pi\beta^2}\right)^{3/2}\left(\frac{heZV\left|\eta\right|^3}{8\pi^3(A\gamma E_0)^3}\right)^{1/4}, \tag{50}$$

where A is the ion atomic number; Z — the ion charge state; h — the harmonic number; $\beta = v/c$; $\gamma = E/E_0$; η — the slip factor; ϕ_S — the synchronous phase; N_b — the number of particles in the bunch; V_{RF} — the accelerating voltage; I_{peak} — the peak current; I_b — the average beam current; S — the normalized longitudinal emittance; σ_ϕ — the RMS phase length of the bunch,

$$I_b = \frac{N_b e Z \omega_0}{2\pi}. \tag{51}$$

The most dangerous is the region of transition crossing, where the Landau damping due to revolution frequency spread becomes equal to zero (at $\gamma = \gamma_{\mathrm{tr}} \rightarrow \eta = 0$). The growth rate in the absence of the Landau damping is [53]

$$\frac{1}{\tau_{\parallel}} = \left(\frac{eZI_b\left|\eta Z_{\parallel}\right|n}{2\pi\beta^2 A\gamma E_0}\right)^{1/2}\omega_0. \tag{52}$$

At transition the growth is mostly driven by the space-charge impedance.

An example of longitudinal microwave instability is shown in Fig. 19.

Longitudinal microwave instability is fast but not destructive. It leads to beam heating — increase of energy spread and bunch length.

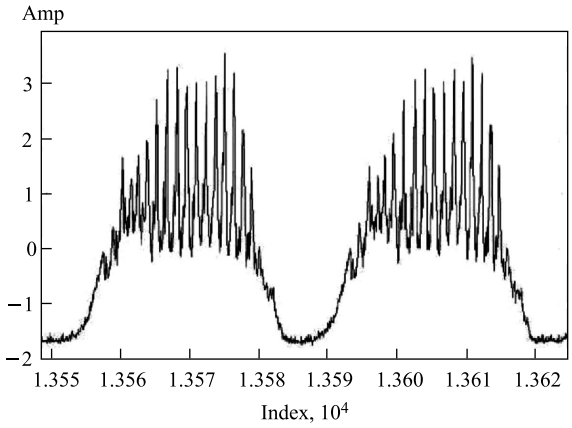

Fig. 19. Longitudinal microwave instability in PSR [75]

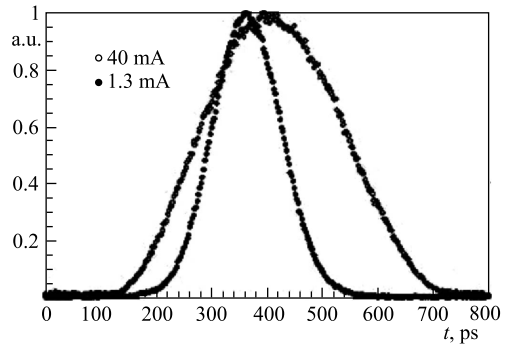

Fig. 20. Bunch density profiles at low and high current in DAFNE [69]

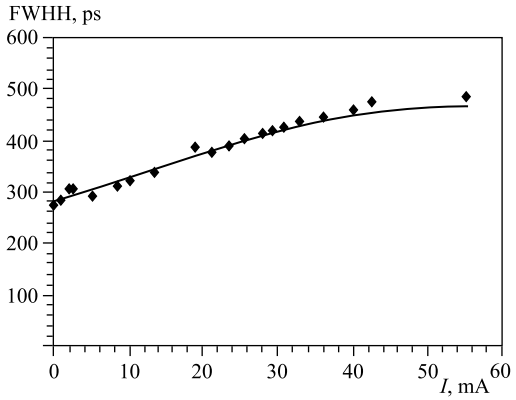

Fig. 21. Bunch length versus current in DAFNE [19]

The bunch length starts to increase from the zero current. After the threshold current, it grows with 1/3 power of the current (Figs. 20, 21).

As for the energy spread, it is almost constant up to the threshold current after which it starts to increase with 1/3 power of the beam current.

In transverse direction, the stability criterion is [13]

$$|Z_\perp| \leqslant 4\sqrt{2\pi}\,\frac{E_0\,AQ\beta\gamma}{e\,ZRI_{\rm peak}}\left(\frac{\Delta p}{p}\right)|(n-Q)\eta-\xi|, \tag{53}$$

where ξ is the chromaticity; R — the machine radius; Q — the betatron tune.

In the transverse case, the Landau damping is due to the revolution frequency spread through the slip factor η and to the betatron tune spread through the chromaticity ξ. At transition, the above threshold is still finite due to the chromaticity.

As the wavelength of the perturbation must be smaller than the bunch length, the minimum value of the harmonic number $n_{\min}$ is

$$n_{\min} = \frac{2\pi}{\omega_0 \sigma_\tau}, \tag{54}$$

where σ_τ is the RMS bunch length in s.

The maximum value of the harmonic number is determined by the pipe cut-off frequency

$$n_{\max} = \frac{c}{\omega_0 b}. \tag{55}$$

The transverse microwave growth rate in the absence of the Landau damping for the broadband impedance is [13]

$$\frac{1}{\tau_\perp} = \frac{eZI_b c Z_\perp}{4\pi Q A \gamma E_0}. \tag{56}$$

In RHIC, the microwave instability limits the longitudinal coupling impedance within the frequency range from the average bunch spectrum frequency of 400 MHz to the beam pipe cut-off frequency of 3.3 GHz to 1.5 Ω (gold ions). At high intensity, the RHIC collider exhibits a fast transverse instability just after transition. By now, the nature of this instability is not quite clear. A hypothesis was put forward that in addition to the coupling impedance an electron cloud effect is involved, too.

For typical values of momentum spread $\sim 10^{-3}$ in order to avoid the MWI the beam intensity should be less than the space charge limit.

Analytical and simulation studies for SIS-100 show that the space charge impedances exceed the threshold of microwave instability both in longitudinal and transverse directions. In SIS-100, feedback system will be used to suppress coherent instabilities.

4.2. Transverse Single-Bunch Instability (Head-Tail Instability). This kind of instability acts in transverse direction. There is no threshold but characteristic growth time. The growth time may be very long in which case the instability will never be seen.

The head-tail instability couples the longitudinal and the transverse motion [24–27, 29, 30, 33, 40, 54, 56]. This perturbation will drive the transverse oscillations of the particles in the bunch tail through the coupling impedance provided the particles in the bunch head receive small transverse displacement. Half a synchrotron period later, these particles swap their positions. Under some conditions a positive feedback could be created and the amplitude of the transverse oscillations starts to grow.

The transverse growth rate for the dipole mode ($m = 0$) is [26]

$$\frac{1}{\tau_0} = -\frac{eZ\,cI_b}{2\omega_\beta\, AE_0 \tau_L} \operatorname{Re}\left[\, Z_\perp(\omega_\xi)\right], \tag{57}$$

where ω_β is the angular frequency of the betatron oscillations; τ_L — is the full bunch length in s, 4σ for Gaussian bunches,

$$\omega_\xi = Q\omega_0 \frac{\xi}{\eta}. \tag{58}$$

The instability shown in Fig. 22 is produced by the interaction of the bunch with the resistive wall impedance (Fig. 23).

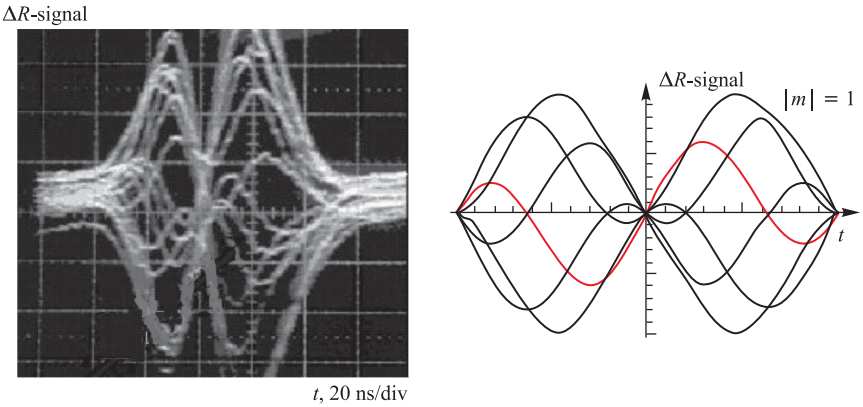

Fig. 22. Head-tail mode $m = 1$ in CERN PS [40]

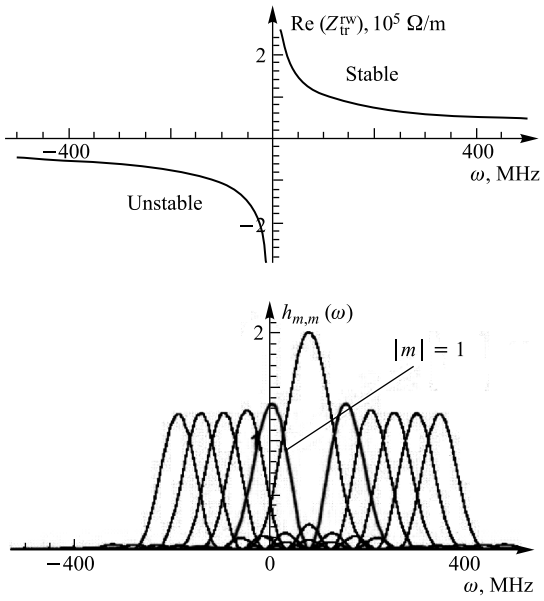

Fig. 23. Mechanism of the head-tail instability with azimuthal mode number $m = 1$ [40]

Below transition $\eta < 0$ and if the chromaticity is negative, than $\omega_\xi > 0$, i.e., we have stability. Above transition $\eta > 0$ and if the chromaticity is positive, than $\omega\xi > 0$, i.e., we have stability. Roughly speaking, for stability the chromaticity must be a few units negative below transition and a few units positive above transition.

In RHIC, the head-tail instability was observed during 2001 Au-run. This was cured making the chromaticity negative below transition and positive above it. Hence the chromaticity must go to zero at transition crossing which means loss of the Landau damping. To ensure that some betatron tune spread exists at transition, the octupoles are used which introduce tune spread with betatron amplitude.

5. COUPLED-BUNCH INSTABILITIES

5.1. Longitudinal Coupled-Bunch Instabilities. Longitudinal coupled-bunch modes are dominated by the resonant impedance (narrow band) [8, 11, 16, 24–27, 29, 30, 33, 52]. Such impedance is due to parasitic higher order modes (HOM) in the RF cavities. In this case, the attenuation of the wake field between two successive bunches is weak — the environment can memorize the passing of a bunch longer than the bunch repetition period. For M equally spaced bunches only every Mth line occurs in the spectrum:

$$\omega_p = (s + pM)\,\omega_0 + m\,\omega_s + \Delta\omega_{\rm cm}, \tag{59}$$

where $p = \ldots, -1, 0, +1, \ldots$ is an integer; $m = 1, 2, 3, \ldots$ is the so-called synchrotron mode ($m = 1$ for the dipole mode, $m = 2$ for the quadrupole mode etc.), $s = 0, 1, \ldots, (M-1)$ is the so-called coupled-bunch mode number. The number s specifies how the individual bunch modes are lined together. The phase shift between oscillations in successive bunches is $2\pi s/M$. In (59), $\Delta\omega_{\rm cm}$ is the coherent frequency shift. This is a complex number. Its imaginary part determines whether the motion is stable or unstable.

HOM in the cavities are the main source of coupled-bunch instabilities in cyclic accelerators. The growth rate is the highest when the cavity modes coincide with the synchrotron sidebands of the revolution frequency.

The growth rate of the longitudinal coupled-bunch instabilities without taking into account the Landau damping effect is [26]

$$\frac{1}{\tau_{\rm ms}} = \frac{\eta\, e^2 N_b M R_{\rm sh}\omega_r}{2\beta^2 E_0 \omega_s T_0^2}\, \tilde{F}_m(\Delta\phi)\, D\,(\alpha\tau_{\rm sep}), \tag{60}$$

where η is the slip factor; ω_S is the synchrotron frequency; N_b is the number of particles per bunch; M is the number of bunches; m is the single-bunch mode number in the longitudinal phase space ($m = 1$ denotes dipole mode, $m = 2$ —

quadrupole mode, etc.); $R_{\rm sh}$ is the shunt impedance of the resonator HOM; ω_r is resonant frequency of the HOM; $\tilde{F}_m$ is a form factor and D is the attenuation factor. The form factor $\tilde{F}_m$ is a function of $\Delta\phi = 2\omega_r\hat{\tau}$ — the change in phase of the resonator during the passage of the bunch, $\hat{\tau}$ being the half-bunch length. In (60), $\alpha = \omega_r/2Q$ is the resonator bandwidth (for narrow resonance $\alpha \ll \omega_r$) and $\tau_{\rm sep} = T_0/M$ is the bunch separation.

The form factor $\tilde{F}_m$ is calculated numerically and depicted in Fig. 24.

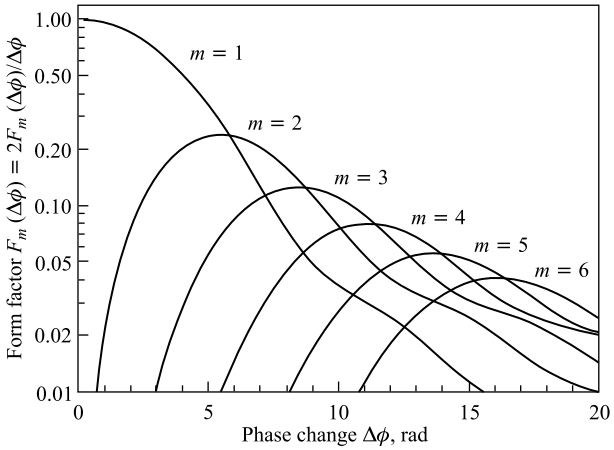

Fig. 24. Longitudinal form factor for the coupled-bunch instability [26]

The growth rate can be expressed also in the form:

$$\frac{1}{\tau_{\rm ms}} = -\frac{nI_bM\omega_sR_{\rm sh}}{2hV_{\rm RF}\cos\phi_S}\,\tilde{F}_m(\Delta\phi)\,D(\alpha\tau_{\rm sep}), \tag{61}$$

where $I_b = eN_b/T_0$ is the average bunch current; $V_{\rm RF}$ is the accelerating RF voltage and ϕ_S is the synchronous phase. In (61) n is the positive harmonic number nearest to the high-Q resonator HOM frequency.

It could be shown that for narrow resonance, when $\alpha\tau_{\rm sep} \ll 1$ and the coupled-bunch mode $s \neq 0$ or $M/2$ (the later for M even), when the resonant frequency of the HOM is at the upper synchrotron sideband: $\omega_r = (pM+s)\,\omega_0 + m\omega_s$ the attenuation factor is equal to unity, $D = +1$. On the other hand, when the resonant frequency is at the lower synchrotron sideband: $\omega_r = (pM-s)\,\omega_0 - m\omega_s$ the attenuation factor is equal to minus unity, $D = -1$. This means that above transition energy the upper synchrotron sidebands generate instability, while being below transition energy they generate stability (Fig. 25).

For $s = 0$ or $M/2$ (the later for M even) both lower and upper synchrotron sidebands belong to one and the same coupled-bunch mode. So in this case, both

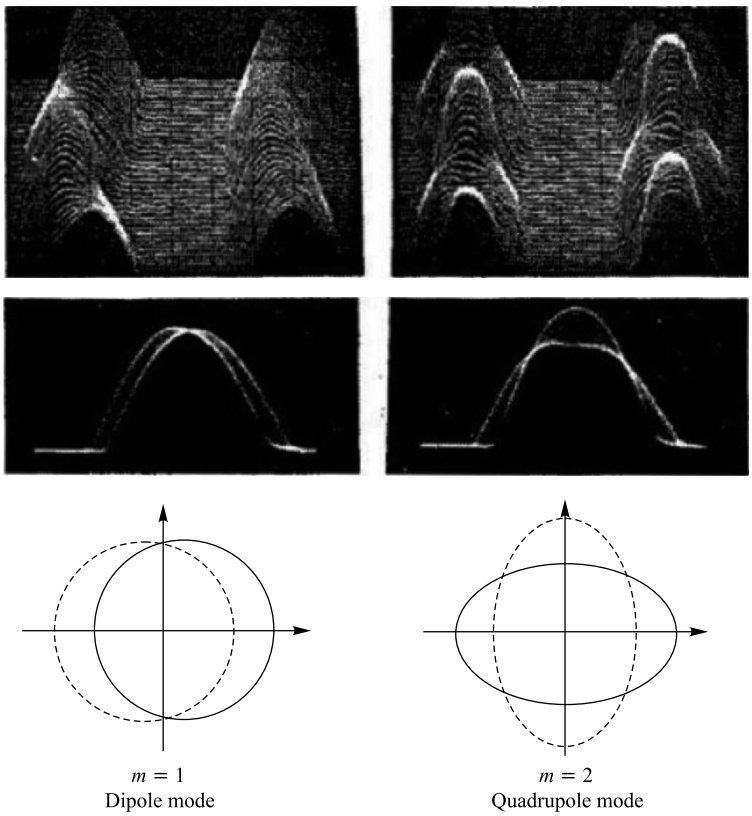

Fig. 25. Dipole and quadrupole coupled-bunch modes in CERN PSB [38]

lines will contribute to the induced by the HOM instability. In this particular case Robinson's criterion works [12]:

$$\frac{1}{\tau_m} \sim -\frac{I}{V \cos \phi_S} [\mathrm{Re}\,(Z_\parallel(n\omega_0 + m\omega_s)) - \mathrm{Re}\,(Z_\parallel(n\omega_0 - m\omega_s))], \tag{62}$$

where n is the harmonic number closest to the resonant frequency. The Landau damping effect may stabilize the beam dynamics.

5.2. Transverse Coupled-Bunch Instabilities Driven by Resistive Wall Impedance. In transverse direction when we work with both positive and negative frequencies ($p = -\infty, \ldots, +\infty$), the bunch spectrum is a line spectrum at

$$\omega_p = (pM + Q + s)\omega_0 + m\omega_s, \tag{63}$$

where $s = 0, 1, \ldots, (M-1)$ is the coupled-bunch mode number.

If we work only with positive frequencies ($p = 0, 1, 2, \ldots$), the transverse spectrum of the bunch is at the so-called upper and lower synchrotron sidebands around upper ($(p + Q)\omega_0$) and lower ($(p - Q)\omega_0$) betatron sidebands of the revolution harmonics ($p\omega_0$):

$$\begin{aligned} \omega_p^+ &= (pM + Q + s)\,\omega_0 + m\omega_s, \\ \omega_p^- &= (pM - Q - s)\,\omega_0 - m\omega_s. \end{aligned} \tag{64}$$

In transverse direction, the power spectrum is centered at chromatic frequency $\omega_\xi = (\xi/\eta)\,\omega_0$. This is the fundamental difference between the transverse and the longitudinal directions.

The most serious coupled-bunch instability in transverse direction is driven by the resistive wall impedance [24–27, 29, 30, 33, 40, 59, 61, 64, 71].

The real part of the resistive wall impedance, $\mathrm{Re}\, Z_\perp^{\mathrm{rw}}$, is inversely proportional to the square root of the frequency. It is peaked at close to zero frequencies. Also $\mathrm{Re}\, Z_\perp^{\mathrm{rw}}$is positive for positive frequencies and negative for negative frequencies. For that reason, the transverse coupled-bunch instability is driven by the spectrum line from the negative frequencies region which is closest to the origin (dominant line) (Fig. 26).

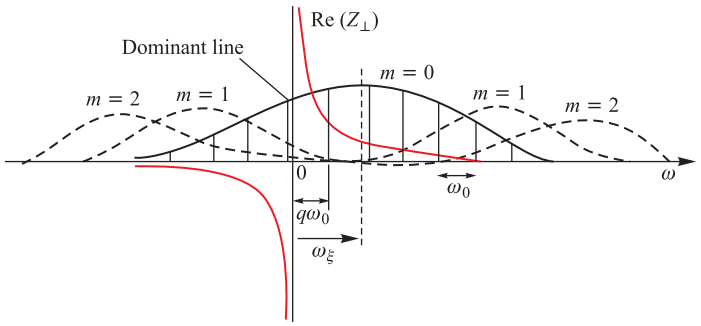

Fig. 26. Transverse coupled-bunch instability driven by resistive wall impedance [38]

The growth rate is given by [26]

$$\frac{1}{\tau_{ms}} = -\frac{1}{1+m}\,\frac{eMI_b c}{4\pi Q E_0}\,\mathrm{Re}\, Z_\perp^{\mathrm{rw}}(\omega_p)\, F'_m(\omega_p \tau_L - \chi), \tag{65}$$

where I_b is the current of one bunch; τ_L is the full bunch length in s; q is the fractional tune and $\chi = \omega_\xi \tau_L$. The form factor $F'_m(\omega_p \tau_L - \chi)$ is shown in Fig. 27.

For zero chromaticity, only the dipole ($m = 0$) mode can be unstable as the quadrupole and the higher-order modes are picked at high frequencies where the resistive wall impedance is very small.

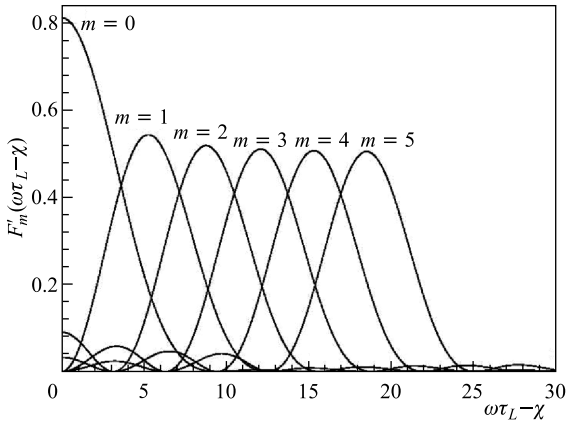

Fig. 27. Transverse form factor for the coupled-bunch instability [26]

For long bunches and above transition the dipole mode could be made stable introducing a positive chromaticity, but in this case the quadrupole mode could still remain unstable. Even for $\xi = 0$ and short bunches if we choose the betatron tune Q just above an integer (the fractional part of the tune $q < 0.5$), the motion will be stable as the damping line at $+q\omega_0$ will act stronger than the antidamping line at $(q-1)\,\omega_0$. A more effective way of stabilizing the accelerator is through the Landau damping mechanism. The necessary spread of the betatron frequencies could be introduced using octupoles.

5.3. Transverse Coupled-Bunch Instabilities Driven by HOM in Accelerating Cavities. Parasitic transverse higher-order modes in accelerating cavities could be the source of transverse coupled-bunch instabilities [24–27, 29, 30, 33, 40, 59]. The analysis is similar to that in the longitudinal direction.

For $s = 0$ and $s = M/2$ modes (the later for the case of M even), both lower and upper betatron sidebands correspond to the same coupled-bunch mode and therefore will contribute to the growth rate [26]:

$$\frac{1}{\tau_{\rm ms}} = \frac{1}{1+m}\,\frac{eMI_bc}{4\pi QE_0}\big[\mathrm{Re}\,Z_\perp^{\rm HOM}((pM-Q-s)\omega_0 - m\omega_s)\times$$
$$\times F'_m(((pM-Q-s)\omega_0 - m\omega_s)\,\tau_L - \chi) - \mathrm{Re}\,Z_\perp^{\rm HOM}((pM+Q+s)\omega_0 + m\omega_s)\times$$
$$\times F'_m(((pM+Q+s)\omega_0 + m\omega_s)\,\tau_L - \chi)\big]. \quad (66)$$

Equation (66) is an analog to Robinson's criterion in the transverse phase plane. If the resonant frequency is closer to the lower betatron sideband, there will be instability, and when it is closer to the upper betatron sideband, there will be damping of the coherent perturbation.

For the other $(M-2)$ modes, the upper and lower betatron sidebands correspond to different coupled-bunch modes. In these cases only one of the sidebands will be close to the resonant frequency and will contribute. In this case, the growth rate is given by [26]

$$\frac{1}{\tau_{\rm ms}} = \pm \frac{1}{1+m} \frac{eMI_b c}{4\pi Q E_0} [\mathrm{Re}\, Z_\perp^{\rm HOM}(n\omega_0)\, F'_m(n\omega_0\tau_L - \chi)], \tag{67}$$

where n is the harmonic number closest to the resonant frequency. The plus sign is when the resonant frequency is at the lower synchrotron sideband which means instability. The minus sign is when the resonant frequency is at the upper synchrotron sideband which means stability.

To stabilize the beam, one must set $\omega_\xi > 0$ which means to set the chromaticity $\xi < 0$ below transition and $\xi > 0$ above transition.

In RHIC, for the longitudinal coupled-bunch instability, the growth rates have been limited by to 2 s^{-1} [49]. To achieve this requirement, higher-order mode dampers have been installed on the RF cavities. Without mode coupling, the growth rate of slow transverse instability has been assessed to be 27 s^{-1}. Increasing the chromaticity above transition and decreasing it below transition can help to cope with the problem.

6. LANDAU DAMPING

There exists a natural mechanism that could stabilize the coherent instabilities — the Landau damping [24]. It originates from the fact that in an accelerator the individual particles oscillate with slightly different frequencies. There are two sources of the Landau damping of the coherent instabilities. The first source is the nonlinearity of the RF focusing force. This nonlinearity leads to dependence of the frequency of synchrotron oscillations on the amplitude $\omega_s(A_\delta)$. This is, for example, the case of a sinusoidal accelerating voltage. The synchrotron frequency spread depends on the bunch and bucket areas. The second source of the Landau damping is the dependence of the betatron tune on the particle energy through the slip factor η and the nonlinearity of the magnetic lattice which cause a dependence of the tune on the amplitude of the oscillations $Q(A_\beta)$. The Landau damping works if the frequency of the coherent instability falls inside the distribution of the incoherent frequencies. The Landau damping mechanism is automatically included in the treatment if we use the Vlasov equation for the stability analysis.

The longitudinal instabilities are Landau damped if

$$\frac{1}{\tau} \leqslant \frac{\sqrt{m}}{4} \Delta\omega_s, \tag{68}$$

where $\Delta\omega_s$ is the spread of the synchrotron frequency due to the nonlinearity of the RF voltage.

Quadrupole and higher-order mode longitudinal instabilities are usually stable if the dipole modes are stable.

For sinusoidal RF voltage:

$$\frac{\Delta\omega_s}{\omega_s} = \left(\frac{\pi^2}{16}\right)\left(\frac{1+\sin^2\phi_s}{1-\sin^2\phi_s}\right)\left(\frac{\tau_L}{T_{\rm RF}}\right)^2. \tag{69}$$

The spread of the synchrotron frequency is shown in Fig. 28.

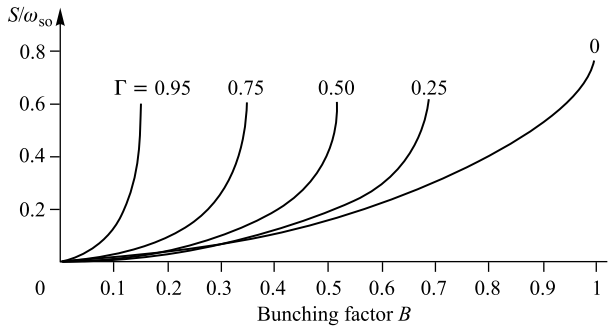

Fig. 28. Synchrotron frequency spread as a function of bunching factor $B \approx \tau_L f_0$ for different values of the parameter $\Gamma = \sin\phi_s$

The Landau damping is especially efficient for long bunches which is the usual case for proton and ion machines.

Momentum spread that is required to stabilize transverse instabilities through the Landau damping mechanism is larger than that which is necessary for damping the longitudinal instabilities.

We can increase the frequency spread and thus enhance the Landau damping adding a higher harmonic voltage to the RF voltage:

$$V_{\rm RF} = V_0 \sin(\omega_{\rm RF} t) + V_N \sin(N\omega_{\rm RF} t). \tag{70}$$

This method was tested in ISR as early as in 1977 [76] introducing the 6th RF harmonic ($N = 6$).

7. COHERENT INSTABILITIES IN THE NICA BOOSTER

7.1. Introduction. The parameters of the NICA booster are as follows [83]:
Accelerating ions ${}_{197}\mathrm{Au}^{32+}$.
Accelerator circumference $C = 211$ m.
Injection energy $T_{\rm inj} = 6.2$ MeV/u.
Energy of electron cooling $T_{\text{e-cool}} = 100$ MeV/u.

Maximum energy $T_{\max} = 600$ MeV/u.
Transition energy $T_{\rm tr} = 3.98$ GeV/u.
Intensity $N = 1.5 \cdot 10^9$.
Beam rigidity
at injection, $B\rho_{\rm inj} = 2.2$ T $\cdot$ m
maximum, $B\rho_{\max} = 25$ T $\cdot$ m.
Magnetic structure: FODO.
Number of periods $N_{\rm per} = 24$.
Number of dipoles $N_B = 40$.
Maximum dipole field $B_{\max} = 1.8$ T.
Field ramprate $dB/dt = 1.2$ T/s.
Effective length of dipoles $L_{\rm eff} = 2.2$ m.
Number of quadrupoles $N_Q = 48$.
Maximum gradient in quads $G_{\max} = +19.7/-20.3$ T $\cdot$ m.
Bending radius $\rho = 14.09$ m.
Betatron tunes $Q_x = 5.8$, $Q_y = 5.85$.
Chromaticity
$\Delta Q_x/\Delta p/p = -6.8$,
$\Delta Q_z/\Delta p/p = -6.5$.
Compaction factor $\alpha = 0.038$.
Acceptance
$A_x = 400\ \pi$ mm $\cdot$ mrad,
$A_y = 70\ \pi$ mm $\cdot$ mrad.
Emittance
at injection $\varepsilon_x = \varepsilon_y = 10\ \pi$ mm $\cdot$ mrad,
at the end of the cycle $\varepsilon_x = 1.7\ \pi$ mm $\cdot$ mrad,
$\varepsilon_y = 2.0\ \pi$ mm $\cdot$ mrad.
Momentum spread
at injection $\Delta p/p = \pm 10^{-3}$,
at the end of the cycle $\Delta p/p \pm 8 \cdot 10^{-3}$.
Accelerating voltage $V_{\rm RF} = 7$ kV.
Accelerating frequency $f_{\rm RF} = 0.6{-}4.4$ MHz.
Synchronous phase $\phi_s = 30^\circ$.
Longitudinal emittance $\varepsilon_L = 3.6$ eV/s.
Duration of the cycle $T_{\rm cycl} = 4.02$ s.

The cross sections of the booster dipole and quadrupole magnets are shown in Figs. 29 and 30.

7.2. Longitudinal Microwave Instability. For small rings (low energy) the coupling impedance is dominated by the space–charge field of the beam itself rather than by the beam-surrounding coupling. As for the real parts of the longitudinal and transverse impedances, they are determined by the resistance of the pipe walls.

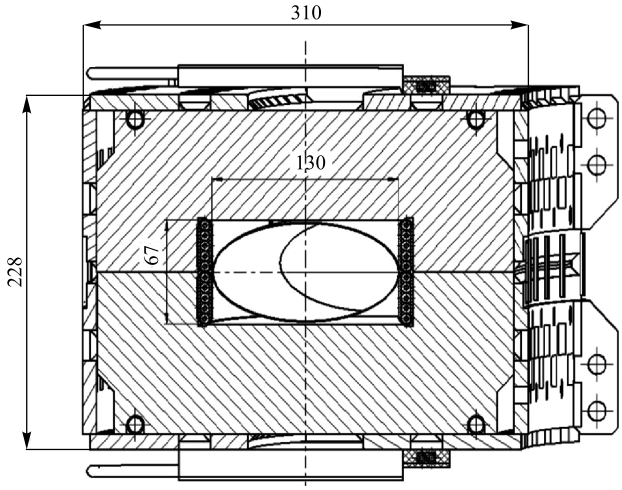

Fig. 29. Cross section of the NICA booster dipole magnet [84]

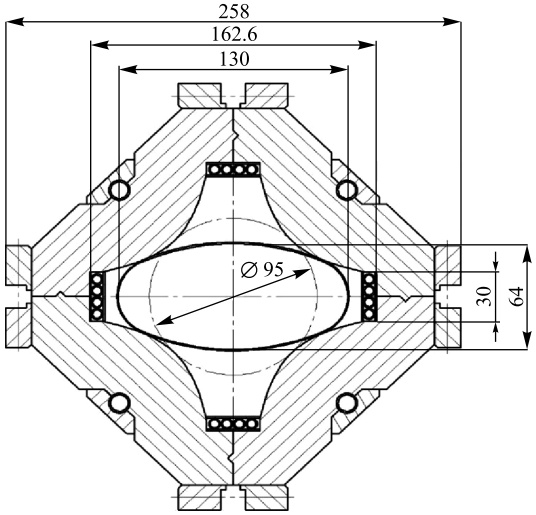

Fig. 30. Cross section of the NICA booster quadrupole magnet [84]

On the other hand, the space–charge forces produce incoherent shift $\Delta Q_{\rm inc}$ of the betatron tunes. The space–charge limit is given by

$$N_{\rm inc} \approx \pi \Delta Q_{\rm inc} \varepsilon_- \left(1 + \sqrt{\frac{\varepsilon_+ Q_-}{\varepsilon_- Q_+}}\right) \beta^2 \gamma^3 \frac{B_f}{G_{\rm inc} r_i}, \tag{71}$$

where ε_- and ε_+ are smaller and larger than ε_H and ε_V, respectively, and Q_- and Q_+ are the corresponding betatron tunes; $\beta c = v_0$ is the ion velocity; B_f is the bunching factor $B_f = \dfrac{I_{\rm peak}}{I_{\rm average}}$; $G_{\rm inc}$ is a form factor between 1 and 1.5; $r_i = \dfrac{(qe)^2}{4\pi\varepsilon_0 A m_u c^2} = \dfrac{q^2}{A}\ 1.544 \cdot 10^{-18}$ m is the classical ion radius.

Combining the microwave threshold limit and the incoherent tune shift we could receive:

$$\left(\frac{\Delta p}{p}\right)^2 \geqslant \sqrt{2\pi}\,\frac{\varepsilon g \Delta Q_{\rm inc}}{h\,|\eta|\,\sigma_L}, \tag{72}$$

where

$$\varepsilon = \varepsilon_V + \sqrt{\varepsilon_H \varepsilon_V}. \tag{73}$$

Numerical estimates show that in longitudinal direction $Z_\parallel/n = -j\,6.35$ kΩ.

a) *Up to Electron Cooling*. The threshold momentum spread for this region was estimated as $\Delta p/p \geqslant 2.7 \cdot 10^{-4}$, so problems are not expected.

b) *Electron Cooling*. The electron cooling will be performed on a coasting beam at energy of 100 MeV/u. The cooling will last up to 1 s.

The frequency of the coherent perturbation $\omega_{\parallel\,\rm pc}$ for monochromatic coasting beams is given by

$$\left(\frac{\omega_{\parallel\,\rm pc}}{p\omega_0}\right)^2 = -j\,\frac{\eta(Z/A)\,I}{2\pi(m_0c^2/e)\,\gamma_0\beta_0^2}\,\frac{Z_\parallel(p)}{p}, \tag{74}$$

where I is the mean current of the beam.

For instability to occur, the imaginary part of the perturbation tune must be negative: $\mathrm{Im}\,(\omega_{\parallel\,\rm pc}) < 0$. If the perturbation tune is real or its imaginary part is positive, the beam will be stable. The growth rate of the instability is determined by the imaginary part of the perturbation tune: $1/\tau = -\mathrm{Im}\,(\omega_{\parallel\,\rm pc})$.

As the NICA booster will work below transition energy ($\eta < 0$), the space charge impedance, which is a negative inductance and which dominates for low energy machines, will not cause instability (Fig. 31).

The same is true for broad-band impedance, which at low frequencies end is constant and inductive: $Z_\parallel^{\rm BB}(p)/p = -j\,R_{\rm sh}\omega_0/\omega_r$.

Instability can be produced by resistive wall impedance which has resistive and reactive parts. But this impedance will be small as the accelerator circumference is relatively small and as it will work at cryogenic temperatures. Moreover, the RW impedance is peaked at low frequencies.

If we regard a coasting beam with some momentum spread, then the well-known Keil–Schnell criterion will determine the stability area [4]:

$$\left(\frac{\Delta p}{p}\right)^2 \geqslant \frac{(Z/A)\,I}{(m_0c^2/e)\,|\eta|\,\gamma_0\beta_0^2}\left|\frac{Z_\parallel(p)}{p}\right|. \tag{75}$$

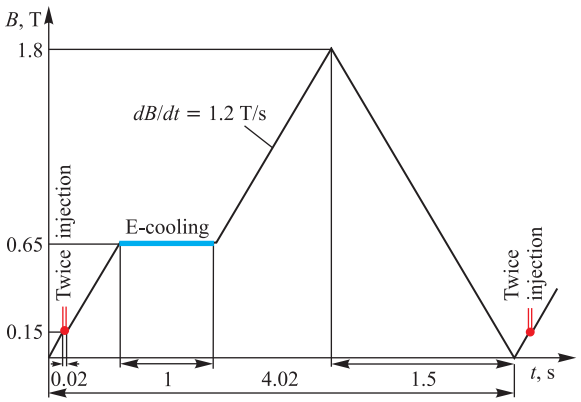

Fig. 31. The magnetic cycle of the NICA booster [83]

From (74) we received the threshold value $\Delta p/p \geqslant 1.32 \cdot 10^{-4}$. The momentum spread which is expected after the electron cooling ($3.8 \cdot 10^{-4}$) is above this threshold.

c) *Acceleration (100 MeV/u → 600 MeV/u).* During this stage the beam is bunched at the first harmonic of the revolution frequency. From (72) we calculated a threshold value for this region to be $\Delta p/p \geqslant 2.6 \cdot 10^{-4}$. The expected momentum spread will lie above this threshold.

7.3. Transverse Head-Tail Instability. In transverse direction the bunch spectrum is centered at chromatic frequency $\omega_\xi = Q\omega_0(\xi/\eta)$. The booster will work below the transition energy and $\omega_\xi = +31.4$ MHz. The spectrum of the dipole mode ($m = 0$) extends to $\pm\pi/\tau_L$. For the NICA booster this means ± 14 MHz.

The transverse head-tail instability is driven by the resistive wall impedance. The transverse resistive wall impedance is sharply peaked at the origin and is calculated by means of (40). For the booster this formula gives

$$R_\perp^{\mathrm{rw}}(\omega) \approx (1+j) \cdot 298.10^6 \frac{1}{\sqrt{\omega}}\ \Omega/\mathrm{m}. \tag{76}$$

The growth rate of the head-tail instability is given by (57). To have an instability, the spectrum of the dipole mode ($m = 0$) must lie in the negative frequency area where the real part of the coupling impedance is negative, i.e., $\mathrm{Re}\,[Z_\perp(\omega_\xi)] < 0 \leftrightarrow \omega_\xi < 0$. In the case of NICA booster, however, due to the natural chromaticity, the spectrum of the dipole mode is centered at relatively high positive frequencies where the real part of the resistive wall impedance is small and positive and we do not expect the transverse head-tail instability to develop.

8. COHERENT INSTABILITIES IN THE NICA COLLIDER RINGS

8.1. Introduction. Variants of the collider rings optics with both constant and variable $\gamma_{\rm tr}$ have been considered [85]. The collider rings are racetracks with two arks and two long straight sections. There are two interaction points. The NICA collider will provide ion–ion and ion–proton collisions in the energy range 1–4.5 GeV/u and collisions between polarized protons and deuterons as well. The magnet structure is based on 2T super-ferric magnets (Figs. 32, 33).

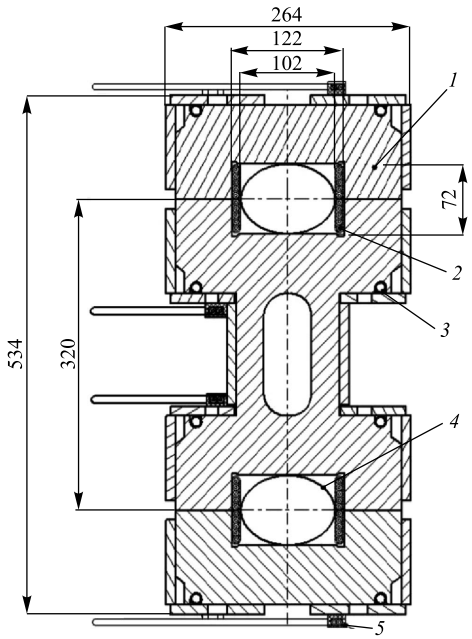

Fig. 32. Cross section of the NICA collider dipole magnet [84]: *1* — iron yoke; *2* — SC winding; *3* — cooling; *4* — beam pipe; *5* — bus bars

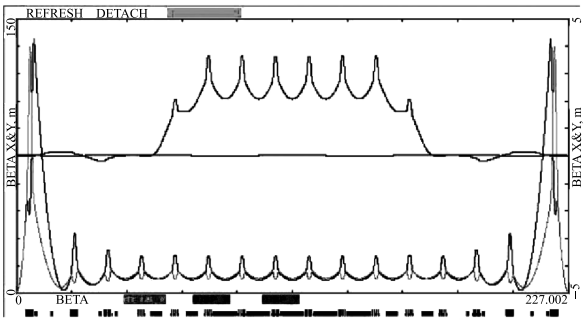

Fig. 33. Optical Twiss functions and dispersion for half of the NICA collider ring [85]

Main parameters of the triplet variant of the rings with fixed $\gamma_{\rm tr}$ are [85]:
Stored ions $_{197}\mathrm{Au}^{79+}$.
Maximum kinetic energy 4.5 GeV/u.
Circumference 454 m.
Transition gamma $\gamma_{\rm tr} = 6.22$.
Betatron tunes $Q_x = 9.46$, $Q_y = 9.46$.
Number of particles per bunch $5.3 \cdot 10^9$.
RMS bunch length 0.6 m.
Number of bunches 20.
Emittances $\varepsilon_x = 1.1\ \pi$ mm $\cdot$ mrad, $\varepsilon_y = 0.6\ \pi$ mm $\cdot$ mrad.
Value of beta function in IP $\beta^* = 0.35$ m.
Maximum magnetic field 2.0 T.
$V_{\rm RF} = 100$ kV (4.5 GeV/u).
$h = 60$.
Intrabeam scattering growth time $\tau_{\rm IBS} = 1350$ s.
Luminosity $L = 6 \cdot 10^{27}$ cm$^{-2} \cdot$ s^{-1} (at 4.5 GeV/u).

Recently a FODO structure of the ring lattice has been considered with 12 cells per arc (90° phase advance per ring) [86].

In my estimations of impedances and instabilities, I have used parameters given in the above table, but the conclusions remain qualitatively valid for FODO-12 structure as well.

8.2. Longitudinal Microwave Instability. The threshold of longitudinal microwave instability of bunched beams has been calculated from (48) to be equal to $|Z_\parallel/n| \leqslant 277\ \Omega$ (at 4.5 GeV/u). On the other hand, the longitudinal space-charge impedance has been estimated from (11) to be $Z_{\parallel\,\rm sc}/n = -j34.4\ \Omega$. The resistive wall impedance is peaked at low frequencies and is of no importance in this case. From (36) the longitudinal resistive wall impedance was estimated to be $Z_\parallel^{\rm rw}/n = (1+j)(2.2/\sqrt{n})$, Ω, where $n = \omega/\omega_0$ is the harmonic number and for the case of MWI n is large. For a well-designed machine the contribution of the BB impedance is of the order of 1Ω. It could be estimated from (24) that for a smooth machine the number of beam pipe transitions per unit length must be $n_{\rm BB}/C = 0.07$ m^{-1}. This means that in order to have less than 10 Ω contribution from the broad-band impedance, the whole number of BB units per ring must be less than 400. Otherwise, the beam pipe transitions should be well tapered and the BB devices well shielded.

The general conclusion is that the longitudinal microwave instability will be of no concern.

8.3. Head-Tail Instability. The head-tail instability has been observed in many machines both electron and hadron or heavy-ion ones. For the dipole mode

($m = 0$), the growth time is given by [26]

$$\frac{1}{\tau_{\rm ms}} = -\frac{1}{1+m}\,\frac{eMI_b c}{4\pi Q E_0}\,[{\rm Re}\, Z_\perp^{\rm rw}(q\omega_0)\, F'_m(q\omega_0\tau_L - \chi) - \\ - {\rm Re}\, Z_\perp^{\rm rw}((1-q)\omega_0)\, F'_m((1-q)\omega_0\tau_L - \chi)]. \quad (77)$$

The above formula for the instability growth rate differs from (57), as in the case of NICA collider rings the bunches are short and therefore the spectrum is wide. In the case of short bunches, the growth or damping of the transverse coherent oscillations depends mainly on two lines $q\omega_0$ and $(-1+q)\,\omega_0$. In the case of NICA collider, the fractional tune q is less than 0.5 and the damping caused by the $q\omega_0$ line overcomes the increase caused by the $(-1+q)\,\omega_0$ line and the overall effect is damping. The only condition is the chromatic frequency to have slightly positive value ($\omega_\xi > 0$) (slightly negative chromaticity, $\xi < 0$). If the sextupole correction is switched off and the collider works at natural chromaticity, the spectrum of the dipole mode will lie deep in the positive frequencies region and the motion will be stable. However, the higher-order modes can still be unstable.

8.4. Longitudinal Coupled-Bunch Instabilities Caused by Parasitic HOM in Accelerating Cavities. The coupled-bunch instabilities in longitudinal direction are caused by the parasitic higher-order modes (HOM) in the RF cavities. The longitudinal impedance of a RF cavity is

$$Z_\parallel(\omega) = R_{\rm sh}\frac{1}{1 + jQ\,\dfrac{\omega^2 - \omega_r^2}{\omega\omega_r}}, \quad (78)$$

where $R_{\rm sh}$ is the cavity parasitic mode shunt impedance; Q is the quality factor, and ω_r is this resonant-mode frequency.

For frequencies close to ω_r:

$$Z_\parallel(\omega) = R_{\rm sh}\frac{1 - j2Q\dfrac{\Delta\omega}{\omega_r^2}}{1 + \left(2Q\dfrac{\Delta\omega}{\omega_r}\right)^2}. \quad (79)$$

The stationary longitudinal spectrum is a line spectrum at harmonics of the revolution frequency $\omega_p = pM\omega_0$, $p = \ldots, -1, 0, +1, \ldots$ (for M equally spaced bunches). The stationary spectrum is peaked at zero frequency and extends to $\pm 2\pi/\tau_L$, where τ_L is the full bunch length in s, 4σ for Gaussian bunches, The spectrum of the perturbation is a line spectrum at frequencies $\omega_p = (pM+s)\omega_0 + m\omega_s + \Delta\omega_{\rm cm}$, where $\Delta\omega_{\rm cm}$ is the coherent frequency shift and determines the stability of the motion. Here, the integer m is the so-called synchrotron mode number, $m = 1$ for the dipole mode, $m = 2$ for the quadrupole mode, etc.

The number $s = 0, 1, \ldots, (M-1)$ is the coupled-bunch mode number. The maximum of the spectrum of longitudinal perturbations falls on $\pm(m+1)\,\pi/\tau_L$ and the main peaks extend to $\pm 2\pi/\tau_L$. Even for the dipole mode the maximum of this spectrum falls in the high frequencies area.

For unstable motion, the driving line must lie in the negative frequencies region. In real world, however, we work only with positive frequencies. This means that for instability to take place, the resonant frequency of the parasitic HOM must coincide with one of the lower synchrotron sidebands of the revolution frequency $p\omega_0 - m\omega_s$, where now $p = 1, 2, \ldots$

If we assume that the shunt impedance of the HOM is $R_{\rm sh} \sim 1$ kΩ, formula (60) gives an exponential growth time of the dipole mode of the longitudinal coupled-bunch instability $\tau \sim 0.6$ s (at 4.5 GeV/u). The existing spread of the synchrotron frequency $\Delta\omega_s$, which is due to the sinusoidal character of the accelerating voltage, can lead to stability of the motion through the Landau damping mechanism according to (66).

The shunt impedance of the higher-order cavity modes could be reduced, if necessary, by means of a passive mode damper. The problem is to damp the HOM without affecting the fundamental (accelerating) mode. HOM dampers are waveguides with a cut-off frequency which is above the fundamental frequency of the cavity.

8.5. Transverse Coupled-Bunch Instabilities Caused by Resistive Walls Impedance. In transverse direction the power spectrum is centered at $\omega_\xi = Q(\xi/\eta)\,\omega_0$ — the betatron frequency shift due to chromaticity. This is the fundamental difference between the transverse and the longitudinal directions. As the collider will work below the transition energy ($\eta < 0$) and the natural chromaticity is negative ($\xi < 0$), the chromatic frequency ω_ξ is positive. This is a line spectrum at frequencies $\omega = (s + pM + Q)\omega_0 + m\omega_s + \Delta\omega_{\rm cm}$, where: $p = \ldots, -1, 0, +1, \ldots$, $m = 0, 1, 2, \ldots$ and $s = 0, 1, \ldots, (M-1)$. For M equally spaced bunches only every Mth line occurs in the spectrum. Synchrotron modes m are no longer sidebands of the Mth revolution harmonics $pM\omega_0$. They are now sidebands of the betatron sidebands, upper: $(pM + s + Q)\,\omega_0$ and lower: $(pM + s - Q)\,\omega_0$. The coupled-bunch mode number s is introduced. This index determines the phase shift between the coherent perturbations in two successive bunches. This phase shift is equal to $2\pi s/M$. The transverse perturbation is coherent only with the synchrotron satellite number m.

It must be pointed out that for the instability to take place, we need $\mathrm{Im}\,(\Omega) < 0$. To fulfill this condition, the resistance must be negative, $\mathrm{Re}\,(Z_\perp) < 0$. In other words, only negative frequency region leads to instability. The instability is driven by the spectrum line ω_p which is closest to the origin of the coordinate system and which lies in the negative frequencies region.

If the collider works with natural chromaticity, the spectrum of the dipole mode ($m = 0$) lies entirely in the positive frequencies region due to the relatively

large and positive chromatic frequency ω_ξ. In this case, the dipole mode will be stable.

If the chromaticity is compensated by means of sextupoles, the dominant line will be $\omega_p = -0.56\omega_0$ ($p = 0$, $s = -10$). For the dipole mode, the growth rate is given by formula (65). This formula gives a growth time of the instability for this case: $\tau = 8$ s (at 4.5 GeV/u).

One method for damping this kind of coupled-bunch instability is to introduce a betatron frequency spread by means of octupoles. The introduced spread must be larger than the growth rate. Another way is to use transverse damping system.

9. MEASURES AGAINST COHERENT INSTABILITIES

Careful design of the circular accelerator is usually sufficient to avoid the coherent instabilities. The vacuum chamber must be as smooth as possible. Any abrupt changes of the vacuum chamber cross section must be systematically tapered and bellows must be shielded. The elements like pick-up electrodes or cleaning electrodes must be properly designed in order to minimize the coupling impedance.

Instead of making an abrupt step between two beam pipes of different radii, it is desirable the aperture transition to be more gradual. For this purpose, a tapered conical section of beam pipe is used. If the aperture transition occurs gradually, the coupling impedance will be significantly reduced. The «five-to-one» rule-of-thumbs states that the taper length must be five times as long as the difference in pipe radii ($\alpha \leqslant 15^\circ$) (Figs. 34, 35).

Unshielded bellows show a broad resonance at a frequency that is a function of the depth of the corrugations. If the bellows are not shielded, they dominate

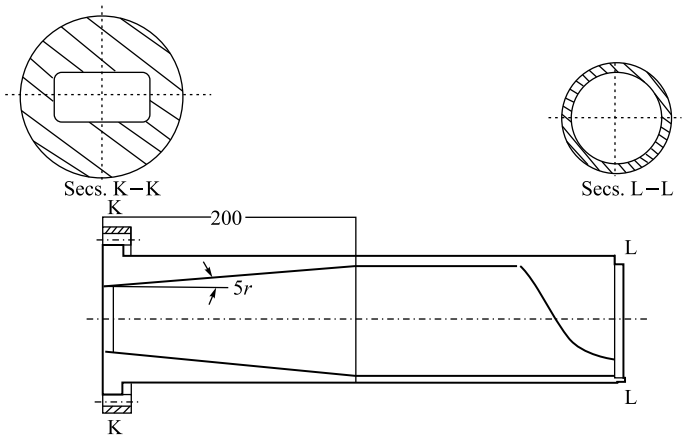

Fig. 34. Cross-section tapers [19]

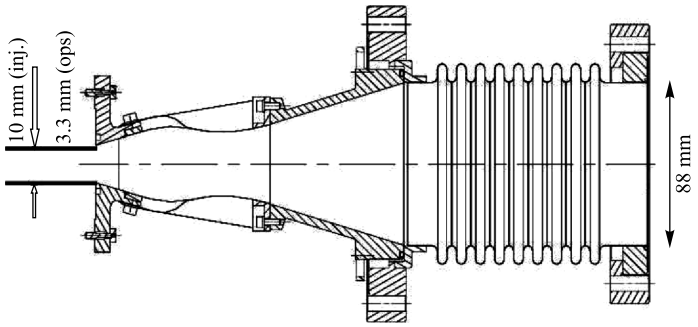

Fig. 35. NSLS MGU taper [78]

the broad-band impedance (BB) (Fig. 36). Usually BPMs, vacuum gate valves, vacuum ports and collimators contribute negligibly to BB impedance.

HOMs in the accelerating cavities are the main source of coupled-bunch instabilities in cyclic accelerators. The growth rate is highest when the cavity modes coincide with the synchrotron sidebands of the revolution frequency. The shunt impedance of the higher-order cavity modes could be reduced, if necessary, by means of a passive mode damper. The problem is to damp the HOM without affecting the fundamental (accelerating) mode. HOM dampers are waveguides with a cut-off frequency which is above the fundamental frequency of the cavity.

For example, in RHIC heavy ion collider two capacitively loaded quarter-wave accelerating cavities are used in each ring. These cavities work at harmonic number 342 and the fundamental frequency is 26.7 MHz. The accelerating voltage is 400 kV per cavity. The data about the fundamental and HOM in the RHIC accelerating cavity are summarized in Table 1.

In RHIC, the impedance limits for HOMs have been determined and passive damping of the higher-order cavity modes has been realized. A broad-band loop-coupled HOM damping system is used. The HOM dampers consist of lumped LC high pass 5th order Chebyshev filter which rejects the fundamental mode while allowing the HOMs to pass (Fig. 37). The cut-off frequency of the filter is

Table 1. **Longitudinal modes in the RHIC accelerating cavity [49]**

f_{RF}, MHz	R_{sh}, MΩ	Q	R/Q, Ω
26.7	0.950	15750	60
103.3	0.129	26880	4.8
192.3	0.077	33430	2.3
276.5	0.174	28850	6.0
328.8	0.307	23260	13.2
394.2	0.156	45160	3.5

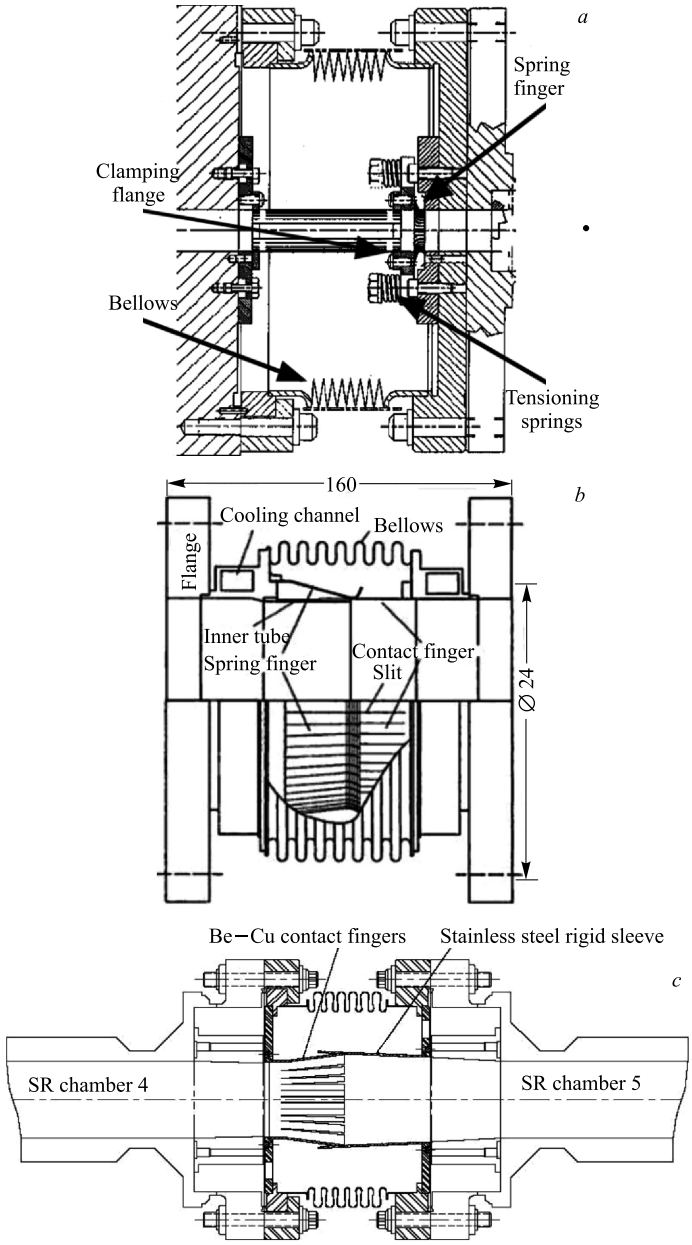

Fig. 36. Bellows shielding [38]

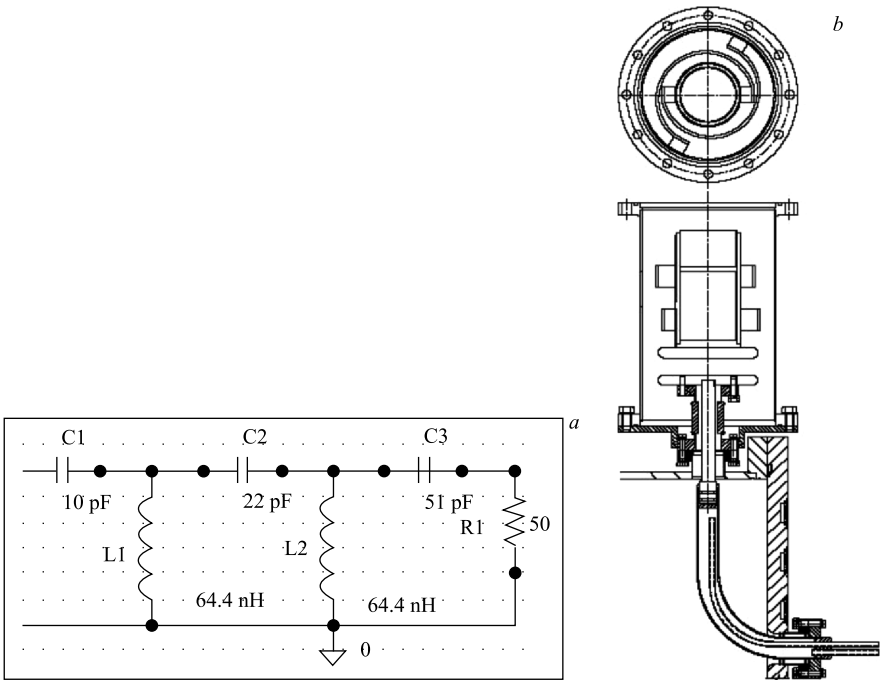

Fig. 37. RHIC HOM damper: *a*) equivalent circuit; *b*) realization [82]

67 MHz. The loops are installed through the enwalls of the cavity and extend up through the cylindrical wall [82].

In hadron machines the Landau damping is usually sufficient to suppress the instability. Unfortunately, this mechanism does not work close to the transition energy.

In the modern accelerators with high intensity beams, feedback systems are used [39, 87–95, 107, 108]. The use of active feedback systems is an effective cure against the coupled-bunch instabilities.

The transverse damping system uses strip-line kickers which can support wide bandwidth and BPMs. Usually, the damping time is set to several hundred revolution periods. Such a system could be used to correct possible injection errors, to excite coherent betatron oscillations in order to measure the betatron tune and to suppress coherent transverse coupled-bunch instabilities. The feedback system must possess sufficient bandwidth to operate on each bunch individually. The necessary power is determined by the expected injection errors and the needed damping rates.

For example, in the RHIC heavy ion collider, the transverse feedback system consists of a beam position monitor located in regions with low dispersion and

a stripline kicker that can support a wide bandwidth. The used power amplifier has a 400 MHz bandwidth which is sufficient to allow operation on each bunch individually. This feedback system could suppress betatron oscillations with amplitude as large as 2 mm. The damping time is equal to 100 turns. The necessary correction kick is 0.4 μrad per turn.

Parameters of transverse feedback systems used in some accelerators are summarized in Table 2.

Table 2. **Parameters of transverse feedback systems used in some accelerators [89]**

Machine	h	M	Mf_0, MHz	Frequency range, MHz	V. I. power	Digital (D) or analog (A)
SPS	4620	4620	200	0.003–10	3 kV	D
PSB	5	5	8	0.005–50	100 W	A
PS	20	20	9.5	0.06–2.5	2 kW	D
FNAL M	1113	1113	53	0–27	5 kW	D
FNAL B	84	84	53	0–27	100 W	A
SPEAR II	280	2	1.3	0–65	2.5 kW	A
NSLS B	5	1	10.5	10–250		A
PETRA	400	80	10.4	5–10	1 kW	D
LEP	31320	$4+4$	0.045	0–23	40 A	D
AA	1	1	1.85	0.1–25	10 W	A
LEAR	1–2	1–2	3.6	0.1–70		A
PEP	2592	$6+6$	0.816	9.4–10.2	20 A	A
ALS	328	328	500	0.15–250	300 W	A
PEPII	3492	1746	238	0.013–238	300 W	A

The damping time of the transverse feedback system is given by

$$\frac{1}{\tau} = \frac{\Delta\theta_{\max}}{2T_{\rm rev}A_{\rm BPM}}\sqrt{\beta_k\beta_{\rm BPM}}, \tag{80}$$

where $\Delta\theta_{\max}$ is the maximum deflection in the transverse stripline kicker; β_k, $\beta_{\rm BPM}$ are the values of the amplitude function in the kicker and in the beam position monitor; $A_{\rm BPM}$ is the amplitude of the oscillations in the BPM.

This damping time must be smaller than the growth time of the coupled-bunch instabilities.

We could write

$$\Delta\theta_{\max} = \frac{V_\perp}{300\beta\, B\rho}, \tag{81}$$

where β is the relativistic factor; $B\rho$ — the beam rigidity in T $\cdot$ m,

$$V_\perp = \int_0^l (\mathbf{E} + \boldsymbol{\beta} c \times \mathbf{B})\, ds \tag{82}$$

is the kick voltage in MV. In (80), l is the length of the kicker.

On the other hand [102],

$$\Delta\theta_{\max} = \frac{2ZelV_k}{AE_0\gamma\,\beta^2 d_k}\tau\eta\alpha, \tag{83}$$

where l is the length of the stripline kicker; $\pm V_k$ is the voltage applied to each plate of the kicker; d_k is the distance between the two plates of the kicker; α is a geometric factor; η is a factor that describes the interaction between the kicker and the beam; τ is the transit time in the kicker

$$\tau = \frac{\sin\,2\omega l/\beta c}{2\omega l/\beta c}. \tag{84}$$

The kicker power is

$$P = \frac{2V_k^2}{R_k}, \tag{85}$$

where R_k is the characteristic impedance of the stripline kicker.

The shunt impedance of the kicker is [111]

$$R_\perp = \frac{V_\perp^2}{2P}, \tag{86}$$

$$R_\perp = 2R_k\left(\frac{2g_\perp l}{d_k}\right)^2\left(\frac{\sin\,kl}{kl}\right)^2, \tag{87}$$

where $g_\perp$ is a geometric factor; k — the wave number.

For the NICA collider we might choose: $lV_k = 200$ V $\cdot$ m, $\tau = 1$, $\eta = 2$, α =1, $d_k = 8$ cm which gives $\Delta\theta_{\max} = 0.74$ μrad.

For amplitude of the oscillation $A = 2$ mm, the damping time will be $\tau = 1.2$ ms, which is enough to damp the transverse coupled-bunch instabilities.

If the characteristic impedance of the stripline is 50 Ω, the necessary kicker power will be 400 W.

The longitudinal feedback system can correct injection errors that lead to dipole (rigid) oscillations of bunches and finally to longitudinal emittance blowup. A longitudinal feedback system will also allow one to damp potential longitudinal coupled-bunch instabilities. The damping time is set usually to several synchrotron periods.

Let us take the longitudinal feedback system in the RHIC heavy ion collider as an example. The RHIC collider has a tight longitudinal emittance budget. The longitudinal damping system is used to correct injection errors. This system corrects the rigid coupled-bunch instabilities. If the bunches from the AGS synchrotron injector are off-centered in the buckets, they will undergo dipole oscillations which leads to longitudinal emittanse blowup. The phase errors during bunch-to-bucket injection are due to the momentum differences between

AGS and RHIC. It is preferable the momentum errors to be less than 10^{-5}. Errors of 10^{-4} will lead to 30% longitudinal emittance blowup. The longitudinal feedback system detects the phase error between the bunch and the bucket centers. The phase errors are then corrected by means of a damping cavity. The damping time is $5\tau_s$ for 1 kV voltage kick. The required power is 10 kW.

Parameters of the longitudinal feedback systems in some accelerators are summarized in Table 3.

Table 3. **Longitudinal feedback systems**

Machine	h	M	Kicker	Frequency, MHz	Power
Mode by mode					
PSB	5	5	RF cavity	3.6–11.2	—
PEP	2592	$3+3$	Special cavity	860	55 kW
NSLS, VUV	9	9	Stripline	400	100 kW
EPA	8	8	Stripline	100	100 kW
SUPER-ACO	24	4	Stripline	400	100 W
FNAL Booster	84	84	?	28 modes/filter	?
Bunch by bunch					
ISR	30	20	RF cavity	9.5	—
PEP	2592	$3+3$	Special cavity	860	55 kW
SppS	4620	$6+6$	RF cavity	200	—
UVSOR	16	16	$\lambda/4$ drift tube	90	100 W
LEP	31320	$4+4$	RF cavity	352	—
ALS	328	328	2-in-series DT	1125	500 W
PEP-II (des.)	3492	1746	3-in-series DT	1012	2 kW

If the bunch was injected off-center in the bucket or if there were momentum errors during injection, the distribution of ions in the longitudinal phase space would start to filament and the longitudinal emittance would blow up. The longitudinal feedback system must be able to correct such errors. It will detect the phase error of the bunch center relative to the center of the RF bucket. Then the signal must be delayed by 90° in the longitudinal phase space and applied to the correcting cavity. The damping rate of the longitudinal feedback system is given by

$$\frac{1}{\tau} = \frac{f_{\mathrm{RF}} \eta V_{\max}}{2(E/eZ)\, \upsilon_s\, \Delta\phi_{\max}} \tag{88}$$

where $\nu_s = \omega_s/\omega_{\mathrm{rev}}$ is the synchrotron tune; $\Delta\phi_{\max}$ is the phase oscillation amplitude; $V_{\max}$ is the maximum correcting kick.

The currently installed feedback systems in CERN accelerator complex are summarized in Table 4.

If for NICA collider we chose $V_{\max} = 1$ kV, injection errors as large as $\Delta\phi_{\max} = 0.06$ rad could be corrected with a damping time $\tau = 0.75$ ms.

Table 4. **Currently installed feedback systems in the CERN accelerator complex [105]**

Accelerator	Digital/analogue processing	Power/kicker/bandwidth	Usage in operation
PS Booster (protons) 50 MeV–1.4 GeV kin. E	Multiturn injection from Linac 2 Analogue beam offset signal suppression, analogue delay (cables & switches)	100 W, 50 Ω stripline limited to 13 MHz in operation but built for 100 MHz bandwidth baseband	H-plane: used and required V-plane: beam stable w/o FB
AD (antiproton decelerator) 3.57–0.1 GeV	Copy of booster system	100 W, 50 Ω stripline 100 MHz bandwidth baseband	Used only for excitation purposes
SPS (protons, ions) 14–450 GeV/c protons FT 26–450 GeV/c LHC beam	Digital notch filter and 1T-delay (Altera FPGA, 80 MHz clock) commissioned in 2000/2001	Tetrode amplifiers with two 30 kW tetrodes in push-pull directly coupled to a kicker (base band); feedback bandwidth $\sim$ 10 kHz to 20 MHz	H-plane: used in operation V-plane: used in operation Used and required for operation above $5 \cdot 10^{12}$ protons (max $\sim 5.5 \cdot 10^{13}$ *ppp* accelerated)
LEIR (ions Pb^{54+}) 4.2–72 MeV/u	Copy of PS Booster System New: remote control of pick-up vector sum	100 W, 50 Ω stripline	2005 Damping during e-cooling may be necessary
PS (protons, ions) 1.4–25 GeV (kinetic E)	Synergy with LHC Damper	3 kW pulsed, 200 W CW, upgrade towards more CW power possible (loads), 112 Ω stripline (0.9 m length), planned with $\sim$30 MHz bandwidth in baseband, lower cut-off $\sim$ 50 kHz. Upgrade possible with magnetic kicker (0.9 m length, 12.5 Ω, but bandwidth considered too limited); H-plane magnetic kicker built already, but BW limited	2006 Injection damping and feedback will be beneficial in particular for high intensity CNGS beams and LHC beams. Currently horizontal instabilities are cured by introducing coupling to the vertical plane which constrains the tunes
LHC (protons, ions) protons 450 GeV/c–7 TeV/c	Digital notch filter and 1T-delay, built-in diagnostics 14 bit ADC/DAC Altera FPGA, 40 MHz clock new development in progress	Tetrode amplifiers with two 30 kW tetrodes in push-pull directly coupled to kicker (base band) similar to SPS system 3 kHz $\rightarrow$ 20 MHz	2007 Injection damping feedback loop closed during ramp switch off during physics?

The nowadays multibunch feedback systems prefer bunch-by-bunch operation to mode-by-mode one. This kind of feedback systems does not require detailed knowledge of instabilities. They are able to stabilize all the coupled-bunch modes by damping the oscillations of each bunch. All the modern feedback systems are digital systems due to the progress in digital electronics. In them, the BPM signal is sampled by an ADC and then processed digitally. The motion of each bunch is measured and a correction signal is applied to the same bunch in a proper phase.

Early feedback systems were analogue ones (Fig. 38).

Nowadays feedback systems are digital. The main constituent blocks of a digital bunch-by-bunch feedback system are shown in Fig. 39.

Detector. It converts the high-frequency BPM signal into the base-band range $(0 - f_{\mathrm{RF}}/2)$.

Stable Beam Rejection. It rejects the revolution harmonics from the correction signal by means of notch filters.

ADC. It converts the analog signal to digital one. Usually 8–12 bit ADCs are used. They sampled and digitize the BPM + Detector signal at bunch repetition frequency (f_{RF}). Precise synchronization of the sampling clock with the bunch signal is necessary.

Digital Signal Processing. It demultiplexes the digital signal to M separated channels. Each channel is dedicated to one of the M bunches in the ring. The individual channels contain digital filters and phase delays.

DAC. Usually 14-bits digital-to-analog converters are used.

Power Amplifier. It works in the base-band frequency range.

Kicker. The transverse kicker is usually a stripline unit. The longitudinal kicker is a cavity structure.

All the components of the feedback system must be integrated into the accelerator control system. One must have opportunity to perform adjustment of the electronics remotely from the control room.

There are several companies that deliver commercial bunch-by-bunch feedback systems. As a rule, this systems use FPGA (Field-Programmable Gate Arrays) DSPs. An FPGA consists of an array of programmable logical block and a reconfigurable interconnection structure that allows the logical blocks to be connected to each other in a way to implement the necessary complex logical functions. The logical blocks contain memory elements. Some FPGAs have integrated ADCs and DACs converting them to programmable systems on a single chip. The modern FPGAs have the ability to be reprogrammed at run time in order to suit better the tack on hand. The biggest companies that manufacture FPGA chips are ALTERA and XILINX [110].

An example is the bunch-by-bunch feedback system «iGp» (Integrated Gigasample Processor) by DIMTEL [103] (Fig. 40).

The bunch-by-bunch feedback system «iGp» uses high-speed ADC and DAC, one turn delay and FPGA processor. The FPGA is driven by the RF clock.

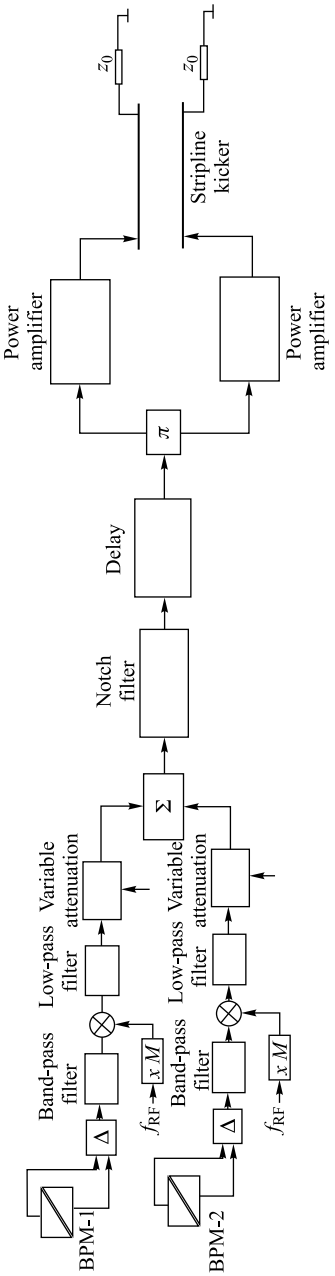

Fig. 38. Principle of an analogues feedback system

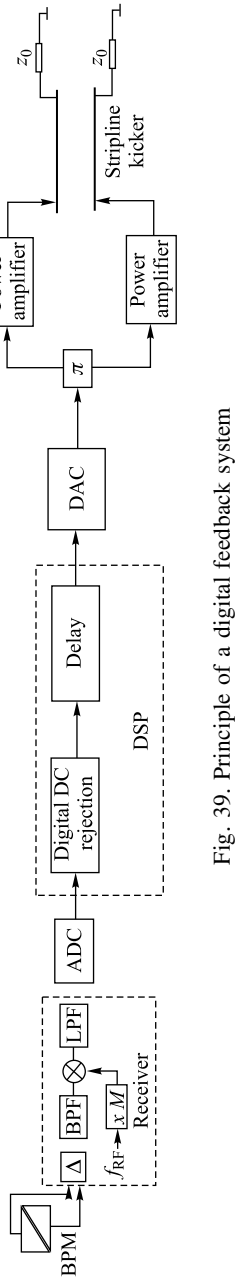

Fig. 39. Principle of a digital feedback system

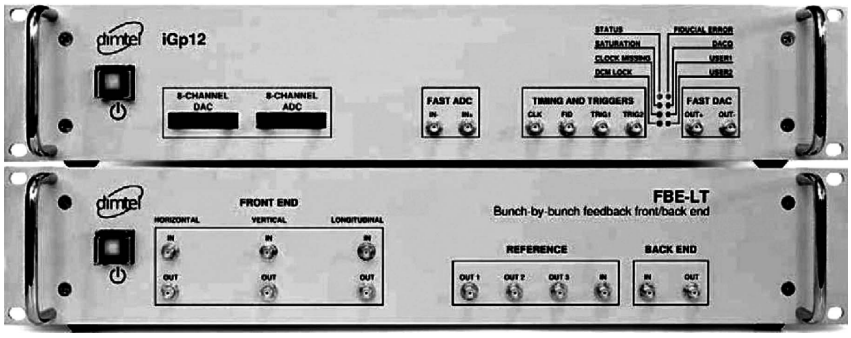

Fig. 40. Integrated gigasample processor (iGp) by DIMTEL [103]

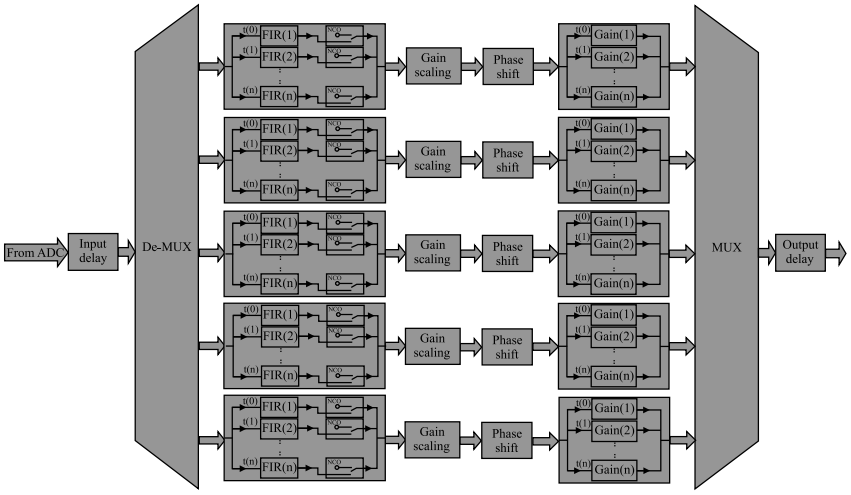

Fig. 41. LIBERA digital signal processing block [104]

The signal from each bunch is processed in a 16-tap FIR (Fixed Impulse Response) filter. The FPGA is connected through USB interface with a computer that runs under Linux and that is connected to the accelerator control system via Ethernet.

Another example is the LIBERA bunch-by-bunch digital processing electronics [104]. In this system the input signal from BPM + Front-End electronics is sampled by one 500 MHz 12-bit ADC. Further the samples are processed bunch by bunch (Fig. 41).

The LIBERA DSP hardware is based on FPGA chips. Digital processing is done separately for each bunch. For this 16-tap FIR filters per bunch are used.

Block-diagram of the LHC transverse damper system is shown in Fig. 42 [105, 106, 109].

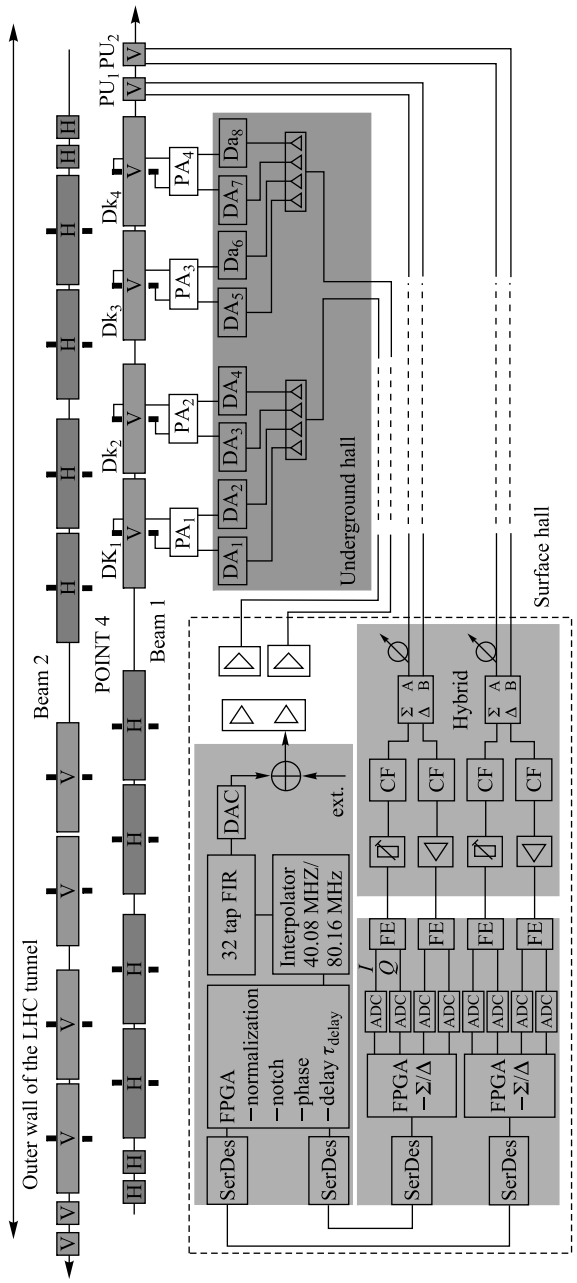

Fig. 42. Block-diagram of the LHC transverse damper system [106]

CONCLUSIONS

The problem of coherent instabilities in the booster and in the collider of the heavy ion accelerator complex NICA is discussed in this paper. The investigation should be looked at as a preliminary study. A more detailed analysis will be performed when the technical design of the accelerator complex will be ready.

In the NICA booster the coupling impedance is dominated by the space-charge field. This kind of impedance is purely reactive — negative inductance. The real parts of the longitudinal and transverse impedances are determined by the resistance of the pipe walls. This impedance will be small as the booster circumference is small and as the accelerator will work at cryogenic temperatures. In addition, the resistive wall impedance is peaked at low frequencies.

Estimations have shown that the booster longitudinal coupling impedance will be relatively small. The expected momentum spread will lie above the threshold of the longitudinal microwave instability.

More specific is the stage of electron cooling, which will be performed on a coasting beam with kinetic energy of 100 MeV/u and will last up to 1 s. The momentum spread that could be reached in the cooling is determined by the condition that the growth time of the instability equals the cooling time.

The booster will work below the transition energy. If no sextupole correction is applied, the spectrum of the transverse dipole mode ($m = 0$) will be centered at relatively high positive frequencies where the real part of the resistive wall impedance is small and positive. The dipole mode of the transverse head-tail instability will see more impedance in the positive frequencies area than in the negative one and the motion will be stable. The higher modes of the transverse head-tail instability however could still be unstable. For achieving stability, larger values of the chromatic frequency ω_ξ will be needed.

In the collider rings, the longitudinal space-charge impedance has been estimated to be $Z_{\parallel\,\mathrm{sc}}/n = -j34.4\ \Omega$. The longitudinal resistive wall impedance would be $Z_\parallel^{\mathrm{rw}}/n = (1+j)\,2.2/\sqrt{n}\ \Omega$, $n = \omega/\omega_0$ being the harmonic number. It will be peaked at low frequencies region. The longitudinal broad-band impedance would be less than 10 Ω provided there would be no more than 400 untapered beam pipe transitions and unshielded BB units per ring.

In longitudinal direction, the coupled-bunch instabilities caused by parasitic higher-order modes in the accelerating cavities would be of potential danger. The exponential growth time of the dipole mode of this kind of instability without the Landau damping has been estimated to 0.6 s.

In transverse direction, the coupled-bunch instability caused by the resistive wall impedance would be dangerous. For the case of compensated chromaticity, the dominant line in the spectrum will be $\omega_p = -0.56\omega_0$ ($p = 0$, $s = -10$). The growth time of the dipole mode has been estimated to 8 s.

The Landau damping phenomenon could be very helpful to cope the instabilities. In transverse direction, the effect of the Landau damping could be enhanced introducing betatron frequency spread by means of octupoles. The introduced spread must be larger than the instability growth rate. In longitudinal direction, the Landau damping mechanism arises from the nonlinear character of the RF focusing force. One could increase the synchrotron frequency spread adding a higher harmonic voltage to the RF voltage.

A careful design of both accelerators will be needed. This includes systematic tapering of any abrupt change in the vacuum chamber cross section and shielding of bellows. Pick-up electrodes should be properly designed to minimize the coupling impedance. As the HOMs in the accelerating cavities are the main source of longitudinal coupled-bunch instabilities, the shunt impedances of the parasitic modes that are most dangerous should be reduced by means of passive dampers.

An effective cure against the coupled-bunch instabilities in the NICA collider will be the use of active feedback systems. Such a system could be used also to correct injection errors and to excite coherent betatron oscillations in order to measure the tunes. Parameters of the transverse and longitudinal damping systems for the NICA collider rings have been estimated in this work. With 400 W power in the transverse kickers, a damping time of 1.2 ms could be realized. In longitudinal direction, a damping time as large as 0.75 ms could be reached with 1 kV voltage kick.

REFERENCES

1. *Vaccaro V. G.* CERN Preprint No. ISR-RF/66-35. 1966.
2. *Sessler A. M., Vaccaro V. G.* CERN Preprint No. 67-2. 1967.
3. *Hubner K., Vaccaro V. G.* Dispersion Relations and Stability of Coasting Beams. CERN Preprint No. ISR-TH/70-44. 1970.
4. *Keil E., Schnell W.* Concerning Longitudinal Stability in the ISR. CERN Preprint No. ISR-TH-RF/69-48. 1969.
5. *Boussard D.* CERN Preprint No. LAB II/RF/INT/75-2. 1975.
6. *Hansen S., Hofmann A.* ISR Performance Report. CERN Int. Report No. ISR-GS/RF-AH/amb. 1976.
7. *Sacherer F. J.* Methods for Computing Bunched-Beam Instabilities. CERN Preprint No. CERN/SI-BR/72-5. 1972.
8. *Sacherer F. J.* A Longitudinal Stability Criterion for Bunched Beams // Proc. of Fifth Particle Accelerators Conf., San Francisco, USA, 1973. P. 825–829.
9. *Sacherer F. J.* Bunch Lengthening and Microwave Instability // IEEE Trans. Nucl. Sci. 1977. V. NS-24, No. 3. P. 1393–1395.

10. *Pellegrini C.* // Nuovo Cim. A. 1969. V. 64. P. 477.

11. *Pellegrini C.* Longitudinal Instabilities in Circular Accelerators and Storage Ring // IEEE Trans. Nucl. Sci. 1981. V. NS-28, No. 3. P. 2413–2419.

12. *Robinson K. W.* Stability of Beam in Radio-Frequency System. Cambridge Report No. CE AL-1010. 1964.

13. *Ruth R. D., Wang J. M.* Vertical Fast Blowup in a Single Bunch // IEEE Trans. Nucl. Sci. 1981. V. NS-28, No. 3. P. 2405–2407.

14. *Krinsky S., Wang J. M.* Longitudinal Instabilities of Long Gaussian Bunches // IEEE Trans. Nucl. Sci. 1983. V. NS-30, No. 4. P. 2495–2497.

15. *Lee S. Y., Zhao X. F.* Microwave Instability in Booster and AGS // Proc. of PAC'1987, Washington, 1987. P. 1188.

16. *Wang J. M.* Longitudinal Symmetric Coupled-Bunch Modes. Brookhaven National Laboratory Report No. BNL 51302. 1980.

17. *Palumbo L., Vaccaro V. G.* Wake Fields, Impedances and Green's Function // CERN Accelerators School, Advanced Accelerator Physics, 1985. V. 1. CERN 87-03. 1987. P. 341–369.

18. *Palumbo L., Vaccaro V. G., Zobov M.* Wake Fields and Impedance. LNF-94/041(P). 1994.

19. *Palumbo L.* Longitudinal Instabilities // CERN Accelerator School, Trieste, 2005.

20. *Zotter B.* Electromagnetic Fields, Impedances and Wakes // AIP Conf. Proc. Phys. of Particle Accel. (N. Y.). 1987. V. 1. P. 663–696.

21. *Zotter B. W., Kheifets S. A.* Impedances and Wakes in High-Energy Particle Accelerators. Singapore: World Sci., 1998.

22. *Ng K. Y., Bane K.* Explicit Expressions of Impedances and Wake Functions. Fermilab-FN-0901-APC. 2010.

23. *Wilson P. B.* Introduction to Wake Fields and Wake Potentials. SLAC-PUB-4547. 1989.

24. *Chao W.* Physics of Collective Beam Instabilities in High-Energy Accelerators. John Willey & Sons, 1993.

25. *Chao A. W.* Coherent Instabilities of a Relativistic Bunched Beam // AIP Conf. Proc. Phys. of High-Energy Particle Accel. (N. Y.). 1983. No. 105. P. 353–523.

26. *Ng K. Y.* Lecture Notes USPAS. Los Angeles, 2002.

27. *Wei J., Fedotov A., Papaphilippou Y.* Physics and Design of High-Intensity Circular Accelerators. BNL, 2002.

28. *Zotter B., Sacherer F.* // Proc. of Intern. School on Particle Accel, Erice, 1976. P. 175.

29. *Moth M., Weng W. T.* Hadron–Hadron Colliders // AIP Conf. Proc. Phys. of High-Energy Particle Accel. (N. Y.). 1983. No. 105. P. 124–280.

30. *Wang J. M.* Modes of Storage Ring Coherent Instabilities // AIP Conf. Proc. Phys. of Particle Accel. (N. Y.). 1987. No. 153. P. 697–788.

31. *Laclare J. L.* Coasting Beam Longitudinal Coherent Instabilities // CERN Accelerator School, Fifth General Accelerator Physics Course. 1992. Geneve: CERN, 1994. P. 349–384.

32. *Laclare J. L.* Coasting Beam Transverse Coherent Instabilities // Ibid. P. 385–408.

33. *Laclare J. L.* Bunched Beam Coherent Instabilities // CERN Accelerator School, Advanced Accelerator Physics. 1985. Geneve: CERN, 1987. P. 264–326.

34. *Gareyte J. L.* Observation and Correction of Instabilities in Circulat Accelerators. CERN SL/91-09 (AP). Geneva, 1991.

35. *Myers S.* Instabilities and Beam Intensity Limitations in Circular Accelerators. CERN SL/97-48 (DI). Geneva, 1997.

36. *Pedersen F.* Feedback Systems. CERN PS/90-49. Geneva, 1990.

37. *Hofmann A.* Introduction to Beam Instabilities // CERN Accelerator School, Trieste, 2000.

38. *Schindl K.* Multi-Particle Effects: Instabilities // CERN Accelerator School, Baden, 2004.

39. *Buffone D.* Introduction to Feedback Systems // CERN Accelerator School, Trieste, 2005.

40. *Metral E.* Transverse Instabilities // CERN Accelerator School, Darmstadt, 2009.

41. *D'yachkov M.* Longitudinal Instabilities of Bunched Beams Caused by Short-Range Wake Fields. PhD Thesis. Univ. of British Columbia, 1995.

42. *Bojko R.* New Concept for Transverse Beam Stability in High-Current Heavy-Ion Synchrotrons. Dissertation. Darmstadt: GSI, 2002.

43. *Salvant B.* Impedance Model of the CERN SPS and Aspects of LHC Single-Bunch Stability. PhD Thesis. Ecole Polytechnique Federale. Lousanne, 2010.

44. *Boussard D. et al.* Collective Effects at Very High Intensity in the CERN-PS // IEEE Trans. Nucl. Sci. 1979. V. NS-26, No. 3. P. 3568–3570.

45. *Ruggiero F. et al.* Summary of the Single-Beam Collective Effects in the LHC // IEEE-1998. P. 107–109.

46. *Bane K.* The Transverse Cavity Impedance in LEP. CERN/ISR-TH/80-48. 1980.

47. *Metral E.* Overview of Impedance and Single-Beam Instability Mechanisms // Proc. of PAC'2005, Knoxville, 2005.

48. *Ng K. Y.* Single-Bunch Instabilities of the RHIC Booster. FNAL Preprint No. TM 1385. Batavia, 1986.

49. *Peggs S., MacKay W. W.* Collective Instabilities in RHIC. RHIC/AP/36. 1994.

50. *MacKay W. W. et al.* Estimation of Collective Instabilities in RHIC // Proc. of PAC'1995, Dallas, Texas, 1996.

51. *Bogacz S. A., Harrison M., Ng K. Y.* Coherent Betatron Instability in the Tevatron // EPAC'88, Rome, 1988. P. 643–645.

52. *Bogacz S. A., Stahl S.* Coupled Bunch Instability in Fermilab Booster — Longitudinal Phase-Space Simulation // EPAC'88. P. 646–648.

53. *Martens M. A., Ng K. Y.* Impedance and Instability Threshold Estimates in the Main Injector. Fermilab-TM-1880. Batavia, 1994.

54. *Ivanov P. M. et al.* Head-Tail Instability at Tevatron // PAC'2003, Portland, Oregon, 2003. P. 3062–3064.

55. *Lebedev V. et al.* Coherent Instabilities at the FNAL Booster // HB'2006, Tsukuba, Japan, 2006. P. 69–73.

56. *Schaaf U. et al.* Impedance and Instability Studies at the ESR // EPAC'92. P. 123–125.

57. Conceptual Design Report (CDR). An International Accelerator Facility for Beams of Ions and Antiprotons. GSI, 2001.

58. *Kornilov V., Boine-Frankenheim O., Hofmann I.* Transverse Collective Instabilities in SIS-100 // Phys. Rev. Special Topics Accel. Beams. 2008. V. 11.

59. *Hanichen L. et al.* Numerical Calculation of Ring Coupling Impedance for Synchrotron Accelerators SIS-18 and SIS-100. GSI Sci. Report. 2009.

60. *Bane K. L. F., Ruth R. D.* Bellows Wake Fields and Transverse Single-Bunch Instabilities in the SSC. SLAC/AP-45. 1985.

61. *Heifets S.* Broadband Impedance of the B-Factory. SLAC/AP-93. 1992.

62. *Chin Y. H., Satoh K.* Impedance Budget for the KEK B-factory // IEEE. 1996. P. 3082–3084.

63. *Boine-Frankenheim O., Kornilov V.* 3D Simulation Studies of Transverse Coherent Instabilities in Long Bunches with Space Charge // PAC'07, Albuerque, 2007. P. 3919–3921.

64. *Rees G. H.* Another Look at Coherent Longitudinal Instabilities of Bunched Beams // EPAC'98, Stockholm, 1998. P. 198–200.

65. *Hanichen L. et al.* Comparison of Analytical and Numerical Results for Broadband Coupling Impedance // PAC'09, Vancouver, 2009. P. 3420–3422.

66. *Tsutsui H.* Longitudinal Impedances of Some Simplified Ferrite Kicker Magnet Models // Eur. Particle Accel. Conf. «EPAC'2000», Vienna, 2000. P. 1444–1446.

67. *Dobbing G. S., Wolski A.* Instability Threshold Calculations for DIAMOND // Ibid. P. 1116–1118.

68. *Ghido A. et al.* DAFNE Broadband Impedance // EPAC'2002, Paris, 2002. P. 1494–1496.

69. *Boine-Frankenheim O., Hofmann I., Kornilov V.* Instabilities and Space Charge Effects in High-Intensity Ring Accelerators // EPAC'2006, Edinburgh, 2006. P. 1882–1886.

70. *Al-Khateeb A. M. et al.* Transverse Resistive Wall Impedances and Shielding Effectiveness for Beam Pipes of Arbitrary Wall Thickness // Phys. Rev. ST-AB. 2007. V. 10. P. 064401.

71. *Calago R. et al.* High Current Superconducting Cavities at RHIC // EPAC'2004, Lucern, 2004. P. 1120–1122.

72. *Lin X., Ko V., Ng C. K.* Impedance Spectrum in the PEP-II RF Cavity.

73. *Hahn H., Blaskiewicz M., Davido D.* Coupling Impedance Measurements of the SNS RF Cavity and Extraction Kicker Magnet // PAC'2003, Portland, Oregon, 2003. P. 3035–3037.

74. *Ng K. Y. et al.* Recent Experience with Inductive Insert at PSR // PAC'2001, Chicago, 2001. P. 2890–2892.

75. *Bramham P. et al.* Longitudinal Instabilities of Bunched Beams in the ISR // IEEE Trans. Nucl. Sci. 1977. V. NS-24, No. 3. P. 1990–1992.

76. *Ng K.-Y.* Shielding the Tevatron Bellows. FNAL Preprint FN-494. 1988.

77. *Podobedov B., Krinsky S.* Transverse Impedance of Tapered Transitions with Elliptical Cross Section // Phys. Rev. ST-AB. 2002. V. 10. P. 074402.

78. *Delle Monache G. O. et al.* DAFNE Shielded Bellows // Nucl. Instr. Meth. A. 1998. V. 403. P. 185–194.

79. *Jones J., Shama S., Bromberek G.* APS SR Flexible Bellows Shield Performance // Proc. of Part. Accel. Conf., N. Y., 1999. P. 3095–3097.

80. *Shaposhnikova E.* Signatures of Microwave Instability. CERN Preprint CERN-SL-99-008HRF. 1999.

81. *Rose J. et al.* RHIC 28 MHz Accelerating Cavity System // Proc. of Part. Accel. Conf. «PAC'01», Chicago, 2001. P. 840–843.

82. *Butenko A. et al.* Design of the Nuclotron Booster in the NICA Project // Proc. of «RuPAC-2010», Protvino, Russia, 2010. P. 68–70.

83. *Hodzhibagiyan H. et al.* Superconducting Magnets for the NICA Accelerator Complex // Ibid. P. 41–43.

84. *Kostromin S. et al.* Lattice of NICA Collider Rings // Proc. of «IPAC'10», Kyoto, 2010. P. 690–692.

85. *Kozlov O. et al.* Design of the NICA Collider Rings // Proc. of Intern. Particle Accelerator Conf., San Sebastian, Spain, 2011. P. 1807–1809.

86. *Pedersen F.* Feedback Systems. CERN-PS-90-49. 1990.

87. *Pedersen F.* Multibunch Feedback // Proc. of the 1992 Factories with e^+/e^- Rings Workshop. Lecture Notes in Phys. V. 425. Springer Verlag, 1994.

88. *Lambertson G.* Beam Bunch Feedback // Proc. of US–CERN–Japan Joint Accelerator School. 1994.

89. *Boussard D.* Cures of Instabilities. CERN 95-06. 1995.

90. *Serio M. et al.* Multibunch Instabilities and Cures // Proc. of Eur. Particle Accelerators Conf. «EPAC'96», Sitges, 1996. P. 148–152.

91. *Lanza M.* Multibunch Feedback Systems // CERN Accelerator School (CAS), Sigtuna, Sweden, 2007.

92. *Tobiyama M.* Beam Feedback Systems // Proc. of Joint US–CERN–Japan–Russia Accelerator School, Russia, 2000.

93. *Teytelman D.* Survey of Digital Feedback Systems in High Current Storage Rings // Proc. of Particle Accelerators Conf. 2003, Portland, Oregon, 2003. P. 318–322.

94. *Bufone D. P.* Overview of Fast Beam Position Feedback Systems // Proc. of Eur. Particle Accelerator Conf. «EPAC'08», Genoa, 2008. P. 1021–1025.

95. *Barry W. et al.* Transverse Coupled-Bunch Feedback in the Advanced Light Source // Proc. of Eur. Particle Accelerator Conf. «EPAC'94», London, 1994. P. 122–124.

96. *Oxoby G. et al.* Bunch-by-Bunch Longitudinal Feedback System // Ibid. P. 1616–1618.

97. *Obina T. et al.* Longitudinal Feedback System for the Photon Factory // Proc. of Particle Accelerators Conf. 2007, Albuquerqne, 2007. P. 233–235.

98. *Bossart R. et al.* Operatrion of the Transverse Feedback System at the CERN SPS // Ibid.

99. *Bulfone D. et al.* Bunch-by-Bunch Control of Instabilities with the ELETTRA/SLS Digital Feedback System // Proc. of ICALEPCS. 2003.

100. *Plouviez E. et al.* Broadband Bunch-by-Bunch Feedback for the ESRF Using a Single High Resolution and Fast Sampling FRGA DSP // Proc. of Eur. Particle Accelerators Conf., Edinburgh, 2006. P. 2976–2978.

101. *Xu J. et al.* The Transverse Damper System for RHIC // Particle Accelerator Conf. 1991. P. 1422–1424.

102. *Teytelman D.* iGp-5120F Signal Processor-Technical User Manual. Dimtel Inc., 2008.

103. *Poucki V. et al.* Combating Multibunch Instabilities with the LIBERA Bunch-by-Bunch Unit // Proc. of Eur. Particle Accelerator Conf. «EPAC'08», Genoa, 2008. P. 1251–1253.

104. *Hofle W.* Transverse Feedback System (LHC Damper) // LHC-LUMI-06 Workshop, Valencia, 2006.

105. *Zhabitsky V. M.* LHC Transverse Feedback System: First Results and Commissioning // XXI Rus. Particle Accelerator Conf., Zvenigorod, 2008. P. 97–100.

106. *Zhabitsky V. M.* // Phys. Part. Nucl. Lett. 2008. V. 5, No. 1. P. 49–53.

107. *Zhabitsky V. M.* Transverse Damping Systems in Modern Synchrotrons // Phys. Part. Nucl. Lett. V. 3, No. 1. P. 58–61.

108. *Baudreeughien P. et al.* LHC Transverse Feedback System and Its Hardware Commissioning // Proc. of Eur. Particle Accelerators Conf. «EPAC'08», Genoa, 2008. P. 3266–3268.

109. *Gorbachev E. V. et al.* Implementing Elements of Digital Transverse Feedback System in Altera FPGA // Proc. of RuPAC, Zvenigorod, 2008. P. 6–8.

110. *Cheng W. et al.* Stripline Kicker Design for NSLS2 Storage Ring // Particle Accelerator Conf., N. Y., 2011. P. 603–605.